ACCELERATION OF HIGH ANGULAR AND SPATIAL RESOLUTION DIFFUSION IMAGING USING COMPRESSED SENSING WITH MULTI-CHANNEL SPIRAL DATA

Merry Mani[1], *Mathews Jacob*[2], *Arnaud Guidon*[3], *Vincent Magnotta*[4], *Jianhui Zhong*[5]

[1]*Department of Electrical and Computer Engineering, University of Rochester, Rochester, NewYork*

[2]*Department of Electrical and Computer Engineering, University of Iowa, Iowa City, Iowa*

[3]*Department of Biomedical Engineering, Duke University, Durham, North Carolina*

[4]*Department of Radiology, University of Iowa, Iowa City, Iowa*

[5]*Department of Biomedical Engineering, University of Rochester, Rochester, NewYork*

Correspondence to :

Jianhui Zhong

University of Rochester Medical Center, Box 648

601 Elmwood Avenue

Rochester, NY 14642-8648.

email: jzhong3@gmail.com

phone number: (585) 273-4518.

Word count : 5004

Figures+ tables count : 10

Running title: Acceleration in combined k-q space with multi-channel spiral data

Abstract

Purpose: To accelerate the acquisition of simultaneously high spatial and angular resolution diffusion imaging.

Methods: Accelerated imaging is achieved by recovering the diffusion signal at all voxels simultaneously from under-sampled k-q space data using a compressed sensing (CS) algorithm. The diffusion signal at each voxel is modeled as a sparse complex Gaussian mixture model. The joint recovery scheme enables incoherent under-sampling of the 5-D k-q space, obtained by randomly skipping interleaves of a multi-shot variable density spiral trajectory. This sampling and reconstruction strategy is observed to provide considerably improved reconstructions than classical k-q under-sampling and reconstruction schemes. The complex model enables to account for the noise statistics without compromising the computational efficiency and theoretical convergence guarantees. The reconstruction framework also incorporates compensation of motion induced phase errors that result from the multi-shot acquisition.

Results: Reconstructions of the diffusion signal from under-sampled data using the proposed method yields accurate results with errors less that 5% for different accelerations and b-values. The proposed method is also shown to perform better than standard k-q acceleration schemes.

Conclusion: The proposed scheme can significantly accelerate the acquisition of high spatial and angular resolution diffusion imaging by accurately reconstructing crossing fiber architectures from under-sampled data.

Keywords: compressed sensing, high angular resolution diffusion imaging, non-Cartesian, incoherent sampling, high spatial resolution, joint reconstruction.

Introduction

Diffusion MRI is a unique and sensitive imaging technique employed to estimate the white matter architecture of the human brain in-vivo (1, 2). This technique characterizes the orientational information of the underlying tissue microstructure by measuring the thermally induced self-diffusion of water molecules in the brain parenchyma (3). This enables identification of white matter bundles in the brain, which has several research and clinical applications.

Conventional clinical diffusion imaging protocols are only capable of achieving voxel volumes in the range of 8-27 mm^3, which are about 2-3 orders of magnitude bigger than the underlying axonal structures (4). Such resolution remains insufficient to fully capture the complex axonal configurations often encountered in many areas of interest such as the highly convoluted gyral white matter or the subcortical fascicles. Partial volume artifacts have been shown to adversely affect the accuracy of the derived anisotropy metrics, while studying these structures (5–7). Diffusion Tensor Imaging (DTI) based tractography results are also severely compromised at such low spatial resolutions (8). High Angular Resolution Diffusion Imaging (HARDI) methods provide a more accurate representation of the underlying geometry and have been shown to perform well in regions of interdigitating fibers. Accurate quantification of diffusion measures also demands high angular resolution (9). However, these HARDI schemes can be prohibitively time-consuming and still may not resolve curved fibers or differentiate crossing from kissing bundles when the spatial resolution is not sufficient. In order to better resolve the fiber structure ambiguity resulting from lower resolutions, simultaneously high spatial and angular resolutions are essential. This requires increased sampling of k-space and q-space resulting in prohibitively long scan times.

Several techniques were introduced to accelerate diffusion imaging in recent years. Fast scan techniques such as fast/turbo spin-echo schemes have been used to reduce the scan times in high spatial resolution diffusion imaging (10, 11). Limited field of view (FOV) approaches were introduced to image a specific brain region with high spatial and angular resolution in a realistic scan time (5). Super-resolution methods (12) and noise reduction techniques (13, 14) may also be considered as acceleration schemes since they circumvent the need to collect multiple averages and/or extra diffusion directions. Most of the above methods rely on the acquisition of the data at Nyquist sampling rate. Recently, several schemes that rely on under-sampling the acquisition space were introduced to accelerate diffusion imaging (15–30). For example, parallel imaging methods under-sample the k-space and rely on data from multiple coils to reconstruct alias-free images at high spatial resolution (15, 16). Partial k-space imaging uses image phase constraints to avoid collecting all of the k-space data (17–20). Similarly q-space acceleration techniques such as half q-space imaging leverages the symmetry characteristics in q-space to significantly under-sample in that domain (21, 22).

Compressed sensing methods (23–30) rely on sparsity of the diffusion signal in various transform domains to reconstruct relevant images from fewer q-space measurements.

The main focus of this paper is to simultaneously achieve high spatial and angular resolution diffusion imaging without compromising the FOV, while maintaining a reasonable scan time. To accelerate the acquisition, we under-sample the combined k-q space jointly and incoherently. We also introduce a joint model-based reconstruction scheme that uses compressed sensing (CS) (31–33) to recover the diffusion orientation distribution function (ODF) directly from under-sampled multi-channel k-space data. This scheme recovers the diffusion signal at all the voxels simultaneously from the k-q data, thus enabling to exploit the spatial regularity (25, 34) of the diffusion signal. We model the multi-modal diffusion weighted MR signal at each voxel as a weighted linear combination of Gaussian basis functions of different orientations. Since the number of fiber bundles that can be recovered from any given voxel is finite at the typical diffusion imaging resolutions, the above model is sparse (35). While the specific diffusion model that we employ is similar to the existing Gaussian mixture model that include an isotropic component (36–38), it differs from the existing model in the following aspect: the coefficients of the Gaussian basis functions are permitted to be complex; the magnitude of the complex coefficients are the volume fractions of the Gaussians. This modification helps to account for the image phase, which is often non-zero and spatially varying due to non-idealities in the acquisition scheme such as B_0 inhomogeneities and motion.

The proposed joint recovery scheme is in contrast to existing two-step methods that first recover the diffusion weighted images from under-sampled k-q data using parallel imaging reconstructions (such as SENSE, GRAPPA etc.) and then fit a diffusion model to the magnitude data (23, 25). In addition to facilitating incoherent k-q space under-sampling, the proposed direct estimation scheme also enables to accurately account for the noise statistics without sacrificing the computational efficiency or global convergence guarantees. Several studies have shown the benefit in accounting for the Rician distribution of the noise in magnitude diffusion weighted imaging (39–41). However, the corresponding algorithms for CS are not guaranteed to converge to the global minimum since the cost function is not convex (39). In contrast, since the noise in k-space is Gaussian distributed, the log-likelihood simplifies to the quadratic data term for the proposed scheme; efficient algorithms guaranteed to converge to global minimum do exist in this setting.

We adapt the multi-shot variable density spiral trajectory (SNAILS) (42) to jointly under-sample k-q space. The object of interest is imaged using a relatively high number of diffusion directions. However, the k-space of each diffusion direction is considerably under-sampled by skipping multiple random interleaves of the multi-shot spiral. We randomize the interleaves that are skipped for the different directions, such that the k-q space is evenly and incoherently under-sampled (Fig. 1(e)). A preliminary version of this work was

published in (43). We extend this work in this paper and validate it using retrospectively under-sampling. Recently two other k-q acceleration methods have been proposed (29, 30) in the context of accelerating DTI.

Methods

Incoherent Under-sampling of k-q Space

Current under-sampling strategies used in diffusion imaging falls into one of the categories illustrated in Fig. 1. We employ the under-sampling strategy illustrated in Fig. 1(e) and will refer to our method as the incoherent k-q scheme from here on. In order to jointly and incoherently under-sample the combined k-q space, we start with a multi-shot variable-density spiral k-space trajectory that can provide the desired high spatial resolution. We incoherently under-sample the k-space of each q-space point by skipping multiple interleaves of the spiral; a set of uniformly spaced interleaves with randomized angular offsets are used to sample each q-space point. Thus, for every k-space location, the q-space is under-sampled and vice-versa. This approach is aimed at collecting high-resolution information from both domains, at the same time reducing redundancy in the k-q sampling. Note that here we introduce the incoherence by randomizing the angular offsets of the spirals for each q-space point. Other ways of inducing incoherence can also be used.

Sparse Diffusion Model

We model the diffusion signal at each voxel using a Gaussian mixture model. Specifically, the diffusion signal consists of one isotropic and several anisotropic diffusion components, with diffusivity d. The anisotropic part of the diffusion is modeled using a cigar shaped tensor having a single dominant direction. Such a tensor having a dominant diffusion direction along the x-axis is assumed to be: $\mathbf{D} = [1700\ 0\ 0; 0\ 300\ 0; 0\ 0\ 300]\times 1e^{-6}$ mm^2/s (23, 25). We define N_{bf} basis direction vectors to adequately cover the q-space. Diffusion tensors $\mathbf{D}_i$ oriented primarily along these basis directions are computed a-priori as follows:

$$\mathbf{D}_i = \mathbf{R}_i \mathbf{D} \mathbf{R}_i^T \text{ for } i = 1, 2, ..., N_{bf}, \quad [1]$$

where $\mathbf{R}_i$ is a rotation matrix that rotates the tensor oriented primarily along x-axis to a tensor oriented primarily along each of the basis directions. The diffusion signal s, measured using diffusion sensitizing parameter b and diffusion gradient orientation $\mathbf{g}$ at a given voxel, can then be modeled as:

$$s(b, \mathbf{g}) = s_0 \{ f_0 e^{-bd} + \sum_{i=1}^{N_{bf}} f_i e^{-b\mathbf{g}^T \mathbf{D}_i \mathbf{g}} \}, \quad [2]$$

where s_0 is the non-diffusion weighted signal, d is the diffusivity for which an appropriate value of 1×10^{-3} mm^2/s is assumed (44, 45), and $\mathbf{D}_i$ is the tensor oriented primarily along each of the basis directions. The exponentials in Eq. [2] form the Gaussian basis functions. We allow the coefficients, f_i, of the Gaussian basis functions to be complex in our model. This allows the model to also capture the phase of the signal (e.g., resulting from magnetic field inhomogeneity and motion). The normalized magnitude values of f_i correspond to the volume fractions of the different components present in the model. For the N_q q-space points measured using the diffusion gradient, $\mathbf{g}_q, q = 1, 2, ..., N_q$, Eq. [2] results in a set of linear equations as follows:

$$\underbrace{\begin{bmatrix} s(b,\mathbf{g}_1) \\ \vdots \\ s(b,\mathbf{g}_q) \\ \vdots \\ s(b,\mathbf{g}_{N_q}) \end{bmatrix}}_{\mathbf{s}} = \underbrace{\begin{bmatrix} e^{-bd} & e^{-b\mathbf{g}_1^T D_1 \mathbf{g}_1} & \dots & e^{-b\mathbf{g}_1^T D_{N_{bf}} \mathbf{g}_1} \\ \vdots & \vdots & & \vdots \\ e^{-bd} & e^{-b\mathbf{g}_q^T D_1 \mathbf{g}_q} & \dots & e^{-b\mathbf{g}_q^T D_{N_{bf}} \mathbf{g}_q} \\ \vdots & \vdots & & \vdots \\ e^{-bd} & e^{-b\mathbf{g}_{N_q}^T D_1 \mathbf{g}_{N_q}} & \dots & e^{-b\mathbf{g}_{N_q}^T D_{N_{bf}} \mathbf{g}_{N_q}} \end{bmatrix}}_{\mathbf{A}} \underbrace{\begin{bmatrix} s_0 f_0 \\ \vdots \\ s_0 f_i \\ \vdots \\ s_0 f_{N_{bf}} \end{bmatrix}}_{\mathbf{v}} . \quad [3]$$

For a given voxel, the set of Eqs. in [3] can be written in matrix formulation as:

$$\mathbf{s} = \mathbf{A}\mathbf{v}, \quad [4]$$

where $\mathbf{s}$ is a vector of length N_q, $\mathbf{A}$ is of size $N_q \times (N_{bf}+1)$ and $\mathbf{v}$ is of length $(N_{bf}+1)$. We normalize the energy of the Gaussian basis vectors, which are the columns of the $\mathbf{A}$ matrix in Eq. [3] so as to give equal weights to the isotropic basis functions as well. Since the diffusion tensors $\mathbf{D}_i's$ are already defined, the only unknowns in the model are the coefficients of each diffusion component. To estimate these unknown coefficients in all the voxels, we stack $\mathbf{s}_i; i = 1, 2, ..., N^2$ along the rows of the matrix $\mathbf{S}$ to form

$$\mathbf{S} = \mathbf{V}\mathbf{A}^T, \quad [5]$$

where $\mathbf{S}$ is the matrix of diffusion weighted images of size $N^2 \times N_q$ and $\mathbf{V}$ is of size $N^2 \times (N_{bf}+1)$; $\mathbf{v}_i$ forms the i^{th} row of $\mathbf{V}$. Then, the q^{th} column of $\mathbf{S}$, denoted by $\mathbf{s}_q$, corresponds to the diffusion-weighted image collected along the q^{th} diffusion direction.

The number of fiber orientations possible in any given voxel in the brain is expected to be finite at the spatial resolution in this study. When some orientations are not present in a voxel, the volume fraction (magnitude of f_i) of those corresponding tensors will be zero. Thus, the above model provides a strictly sparse

representation of the diffusion signal in the brain when the actual diffusivity in a specific voxel matches the parameters assumed in the model. The model can account for small changes in diffusivities that naturally occur in the brain at the expense of sparsity. For example, a broader Gaussian (larger diffusivity) may be well approximated as the linear combination of several narrow Gaussians (smaller diffusivity). Thus, any performance degradation due to mismatched parameters is expected to be graceful. Besides, our experimental results show good reconstructions at a range of accelerations, indicating the utility of this model.

An analytical expression for the diffusion ODF for the model in Eq. [2] is given by (46)

$$\Psi(b, \mathbf{g}_q) = f_0 \frac{d}{4\pi} + \sum_{i=1}^{N_{bf}} f_i \frac{(\mathbf{g}_q^T \mathbf{D}_i^{-1} \mathbf{g}_q)^{-\frac{3}{2}}}{4\pi\sqrt{\det(\mathbf{D}_i)}}. \quad [6]$$

Sparsity-Constrained Reconstruction with Motion Compensation

Since the assumed model provides a sparse representation for the diffusion signal, we use an ℓ_1 regularized reconstruction to recover the sparse coefficients. We propose a joint reconstruction of the ODF coefficients directly from the under-sampled multi-channel k-space data.

Motion during diffusion encoding induces phase errors in diffusion imaging; motion between the shots in a multi-shot spiral acquisition could result in considerable artifacts in the reconstruction, if left uncorrected. We adapt the simultaneous phase correction and SENSE reconstruction method introduced in (47) to recover the images directly from the k-space data. However, instead of reconstructing individual diffusion weighted images, we reconstruct the ODF coefficient images by incorporating the diffusion model matrix $\mathbf{A}$ also in the forward model. We compute the coil sensitivities corresponding to each coil using a sum-of-square estimate from a fully-sampled non-diffusion weighted image that we collect during the scan. We estimate the motion-induced phase errors[1]corresponding to each shot and diffusion direction using the k-space data from the center portion of the self-navigated spiral trajectory; note that this does not require fully sampled k-space data. We compute the composite sensitivity maps, $\mathbf{P}$, as the product of the motion induced phased errors and coil sensitivity profiles as discussed in (47). More rigorous approaches as discussed in (48) can account for any high frequency variations in the motion induced phase errors. Then, the k-space measurement matrix $\mathbf{Y}$ can be modeled as:

$$\mathbf{Y} = \mathcal{H}(\mathbf{V}) + \epsilon, \quad [7]$$

[1]In this study, we ignore the effect of noise in the estimated phase, which is used in the forward model. Further studies are needed to fully understand these effects, which is beyond the scope of the present work.

where $\mathbf{Y}$ is a matrix of size $(N_{\mathrm{i}} \times N_{\mathrm{c}} \times N_{\mathrm{k}}) \times N_q$; N_{k}, N_{i}, and N_{c} are respectively the number of k-space points per interleaf, the number of interleaves, and the number of coil elements. ϵ is measurement noise that is Gaussian distributed. Then, $\mathbf{y}_q$, the q^{th} column of $\mathbf{Y}$ corresponds to the k-space measurement using the q^{th} diffusion direction. The measured k-space data corresponding to the k-space location $\mathbf{k}_i$ on the i^{th} interleaf using coil c for the q^{th} diffusion direction is given by:

$$\mathbf{y}_q(\mathbf{k}_i, c) = \sum_{\mathbf{r}} \mathbf{s}_q(\mathbf{r}) \mathbf{P}_{q,i,c}(\mathbf{r})\, e^{-j2\pi \mathbf{k}_{q,i}^{\mathbf{T}} \mathbf{r}}. \qquad [8]$$

Here, $\mathbf{P}_{q,i,c}(\mathbf{r})$ holds the motion induced phase error weighted by the coil sensitivities, for the voxel location $\mathbf{r}$ for the c^{th} coil, i^{th} interleaf and q^{th} diffusion direction and is part of the image encoding function. The Fourier exponentials are evaluated on the non-Cartesian k-space locations of the spiral interleaves that are played out for the diffusion directions. $\mathbf{s}_q(\mathbf{r})$ is the diffusion signal at voxel location $\mathbf{r}$ for the q^{th} diffusion weighted image. The computation of $\mathcal{H}(\mathbf{V})$ for the q^{th} diffusion direction using Eq. [5] and [8] is illustrated using a block diagram given in Fig. 2 .

For $N_q < (N_{bf} + 1)$, Eq. [7] results in an under-determined system with $N_{bf} + 1$ unknowns in every voxel. We formulate the recovery of the ODF coefficients as a non-linear sparse optimization problem that minimizes the ℓ_1 norm of the coefficients. Since we recover the coefficients in all the voxels jointly, the spatial regularity that exists in the fiber structures in adjacent voxels can be used as an additional constraint. This spatial regularization is imposed on the diffusion images using a total variation (TV) penalty in our final optimization problem:

$$\mathbf{V}^* = \arg\min_{\mathbf{V}} \underbrace{||\mathcal{H}(\mathbf{V}) - \mathbf{Y}||_{\ell_2}^2}_{\text{data consistency}} + \beta_1 \underbrace{\|\mathbf{V}\mathbf{A}^T\|_{TV}}_{\text{spatial regularization}} + \beta_2 \underbrace{\|\mathbf{V}\|_{\ell_1}}_{\text{sparsity penalty}}, \qquad [9]$$

where $||\mathbf{V}\mathbf{A}^T||_{TV} = ||\nabla(\mathbf{V}\mathbf{A}^{\mathbf{T}})||_{\ell_1}$. Since the noise in k-space is Gaussian distributed, we obtain the data consistency term in Eq. [9] as the log-likelihood of the probability distribution function of the data in Eq. [7]. The above cost function being convex, any local minimum is also a global minimum [2]. The iterative re-weighted least squares method that we employ is shown to converge to the global minimum (51, 52).

We implemented the ℓ_1 minimization in Eq. [9] as an iterative re-weighted ℓ_2 norm minimization (53). The resulting convex optimization problem is minimized using a conjugate gradient (CG) algorithm with 100 iterations and 20 re-weightings. Since the Fourier transforms are evaluated on non-Cartesian trajectories,

[2] If the solution is sparse and the operator $\mathcal{H}$ satisfies the null-space property, the global minimum is guaranteed to be unique (49, 50).

CG-NUFFT algorithms are used (54). The current implementation in MATLAB with Jacket on a Linux workstation with NVDIA Tesla GPU takes about 3 hours to converge. Once the optimal coefficients are obtained, the diffusion images and ODF are reconstructed using the forward models defined by Eq. [2] and Eq. [6] respectively.

Datasets for Validation

We use three in-vivo datasets and a simulated data for the validation of the various methods. In-vivo brain data of two healthy adult volunteers were collected in accordance with the Institutional Review Board of the University of Iowa. The first volunteer was imaged on a Siemens TIM Trio 3T MR scanner with maximum gradient amplitude of 45 mT/m and slew rate of 200 T/m/sec using a 12 channel head coil. A variable density spiral sequence with the following specifications was used for the first dataset: FOV = 20cm, with a 192x192 matrix, resulting in an in-plane spatial resolution of 1.04 x 1.04 mm^2. 10 slices were acquired with slice thickness of 2.5 mm using a b-value of 1200 s/mm^2. A single fully-sampled non-diffusion weighted image and 64 fully sampled diffusion-weighted images were collected using 22 spatial interleaves, $\alpha = 8$ and readout duration of 18.6 ms. TE/TR was 61/2500ms, resulting in a total scan time of 60 mins for the full dataset. For a higher b-value acquisition at b = 2000 s/mm^2, the first volunteer was scanned using a variable density spiral sequence with the following specifications: FOV = 20cm, with a 192x192 matrix, resulting in an in-plane spatial resolution of 1.04 x 1.04 mm^2. 10 slices were acquired with slice thickness of 3 mm and a slice gap of 1.5 mm to include slices from the inferior regions of the brain also. A single fully-sampled non-diffusion weighted image and 64 fully sampled diffusion-weighted images were collected using 22 spatial interleaves, $\alpha = 10$ and readout duration of 19.3 ms. TE/TR was 100/2500ms, resulting in a total scan time of 60 mins for the full dataset. A second volunteer was also scanned using the same above parameters, except that 17 slices with a slice thickness of 3 mm and 0.6 mm slice gap were collected to maximize the number of possible slice acquisitions per TR. We did not aim for a full brain acquisition in the current study due to the excessive scan time ($>$2 hours) required to acquire the fully sampled data in such case.

We test the robustness of the reconstruction schemes to noise on a simulated data that resemble the main fiber structures in the human brain. The steps for creating the simulated data are included in the supplementary materials.

Experiments

In the following section, we study the performance of four different acceleration schemes and two different reconstruction schemes by doing a retrospective under-sampling of the in-vivo datasets. We also define

three error metrics for the validation of the various experiments.

Various Acceleration Schemes

1. Proposed method: incoherent k-q under-sampling; joint optimization: The k-q space is jointly under-sampled using the incoherent scheme illustrated in Fig. 1(e). Accelerations of 2, 4, 8 and 11 are tested as follows: to achieve an acceleration factor of R, we choose $22/R$ uniform random spatial interleaves to sample the k-space for each of the 64 diffusion directions. The k-q under-sampled data obtained this way is used to reconstruct the ODF coefficients using the joint recovery scheme given in Eq. [9].

2. k-only under-sampling; two-step optimization: The acceleration comes solely from under-sampling the k-space. $R = 2$, 4, 8 and 11 are tested by using the k-only scheme illustrated in Fig. 1(b). Reconstructions are performed by following the standard two-step procedure. First, the individual diffusion weighted images are reconstructed from the under-sampled data using TV regularization. For the q^{th} diffusion direction, the diffusion weighted image $\tilde{\mathbf{s}}_q$ is reconstructed as:

$$\tilde{\mathbf{s}}_q = \underset{\mathbf{s}}{\operatorname{argmin}} ||\mathcal{J}(\mathbf{s}_q) - \mathbf{y}_q||^2_{\ell_2} + \beta_1 ||\mathbf{s}_q||_{TV}; q = 1, ..., N_q, \quad [10]$$

where $\mathcal{J}(\mathbf{s}_q)$ is computed using Eq. [8]. The ODF coefficients are then recovered from the N_q magnitude diffusion weighted images using sparsity constraint.

$$\mathbf{V}^* = \underset{\mathbf{V}}{\operatorname{argmin}} ||\mathbf{V}\mathbf{A}^T - |\tilde{\mathbf{S}}||^2_{\ell_2} + \beta_2 ||\mathbf{V}||_{\ell_1} \quad [11]$$

3. Q-only under-sampling; two-step optimization: The acceleration comes from under-sampling the q-domain alone. Acceleration by a factor of R is achieved by keeping $64/R$ diffusion directions and fully sampling their associated k-space. We use 32, 16 and 8 diffusion directions, that span the q-space uniformly, to test R =2, 4 and 8 respectively. The same two-step procedure stated in Eq. [10, 11] is used to recover the ODF coefficients from the q-only under-sampled data.

4. Hybrid k-q under-sampling; two-step optimization: Here the acceleration R comes from under-sampling the k- and q-space separately. Acceleration R_k in the k-domain is achieved by under-sampling the k-space using the same set of interleaves for every q-space point. Acceleration R_q in the q-domain is achieved by sampling only a subset of the q-space points. Combined acceleration of $R = 4$ is tested by combining $R_k = 2$ and $R_q = 2$. Combined acceleration of $R = 8$ is tested by combining (i) $R_k = 2$ and $R_q = 4$, (ii) $R_k = 4$ and $R_q = 2$. The two-step scheme in Eq. [10, 11] is used to reconstruct the ODFs from the under-sampled k-q data.

Various Reconstruction Schemes

5. Joint vs two-step magnitude-based schemes: To study the effect of noise on performance of the two reconstruction schemes, complex Gaussian noise is added to the k-space predictions of the simulated data at three noise levels: (i) no noise, (ii) complex Gaussian noise with half the noise variance as that of the in-vivo k-space data, and (iii) complex Gaussian noise with full noise variance as that of the in-vivo k-space data. ODFs are reconstructed using the two reconstruction schemes from the fully sampled data at the three noise levels.

Effect of Under-sampling Patterns on the Reconstruction Schemes

To better understand the effect of the various under-sampling schemes on the reconstruction functional employed, the following experiments are also performed:

6. Uniform k-only under-sampling; joint optimization: The k-space is under-sampled using the pattern shown in Fig. 1(b) and the ODF coefficients are recovered using the joint optimization scheme given in Eq. [9]. Various accelerations are tested on simulated and in-vivo data.

7. Incoherent k-q under-sampling; two-step optimization: The incoherent under-sampling scheme as illustrated in Fig. 1(e) is used to under-sample the k-q space and the ODF coefficients are recovered using the two-step optimization scheme given in Eq. [10, 11]. Various accelerations are tested on simulated and in-vivo data.

Error Metrics for Validation

For the purpose of error quantification, we use the ground truth ODFs for the simulated data. For the in-vivo data, a reference ODF is created from the full dataset consisting of 64 directions and 22 interleaves. We compare the ODFs reconstructed using all the schemes along a fixed set of ($\hat{N}_q$=) 2562 points that are obtained by the 4^{th} order tessellation of an icosahedron. To quantify the error in the reconstructed ODFs, three error metrics are computed. The normalized sum-of-squares error (NSSE) quantifies the deviation of the reconstructed ODF values (Ψ_{rec}) from the reference ODF values (Ψ_{ref}) at all the 2562 points.

$$NSSE = \frac{\sum_{x,y,z,\hat{N}_q} (||\Psi_{\mathrm{ref}} - \Psi_{\mathrm{rec}}||_2^2)}{\sum_{x,y,z,\hat{N}_q} ||\Psi_{\mathrm{ref}}||_2^2}. \qquad [12]$$

Average angular error (AAE) calculates the angular deviation of the ODF peaks from the true ODF peaks.

$$AAE = \frac{1}{N_{\mathrm{voxels}}} \sum_{x,y,z} (\frac{180}{\pi} \arccos(\mathbf{u}_0.\hat{\mathbf{u}})). \qquad [13]$$

Here, $\mathbf{u}_0$ is the true direction of the ODF peak, $\hat{\mathbf{u}}$ is the estimated direction and N_{voxel} is the number of voxels being considered. ODF peaks are determined by comparing each ODF point against all the points

in a local neighborhood defined by a cone of 10 degrees and keeping all values that are greater than 30% of the maximum ODF value. In the case of over/under-estimation of peaks, the reconstructed peaks are first matched with the reference peaks. The angle of the extra/missing peak is also used in finding the average angular error. Rate of false peak (RFP) detection represents the error in the number of ODF peaks reconstructed, where $P_{\rm ref}$ and $P_{\rm rec}$ are the true and estimated number of peaks in each voxel respectively.

$$RFP = \frac{\sum_{x,y,z} (||P_{\rm ref} - P_{\rm rec}||_2^2)}{\sum_{x,y,z} ||P_{\rm ref}||_2^2}. \quad [14]$$

Results

To ensure fair comparison between various methods, β_1 and β_2 are optimized for each algorithm and various settings (such as acceleration levels, b-values). Since a reference dataset is available in all of our experiments, the optimal β_1 and β_2 are obtained by picking the parameters that result in minimum angular error compared to the reference dataset. Our specific choices of β_1 and β_2 are provided in the Table 1 for the various experiments. When a reference dataset is not available, efficient schemes to choose the regularization parameters are available (55, 56). L-surface based methods (57, 58) are employed when two regularization parameters are to be optimized.

Comparison of various under-sampling schemes

Figures 3-8 shows the results from the various experiments done on in-vivo datasets. Figure 3 shows the plots of the three error quantification metrics for the different schemes computed on the in-vivo dataset collected at b= 1200 s/mm^2. These plots show the superior performance of the proposed incoherent k-q scheme with joint reconstruction compared to other schemes. The NSSE error is less than 3%, the average angular error is between 5 to 8 degrees and the rate of false peaks is about 5-8% for the proposed method at all accelerations. The ODFs reconstructed using the various schemes for a region of the brain with abundant fiber crossings are shown in Fig. 4. For a reference, an RGB image of the region is shown in Fig. 4(a) that was obtained from a single tensor fit and weighted by fractional anisotropy (FA) values. The ODFs reconstructed from the fully sampled data as well as the under-sampled data for this region are included in the figure. Visual inspection of the ODFs reconstructed using the different methods show clear differences. Clearly, the ODFs reconstructed using the incoherent k-q scheme using joint reconstruction provide a more accurate reconstruction.

The proposed method was also tested on a higher b-value acquisition. Figure 5 shows the plot of the reconstruction errors from two different slices of the in-vivo data collected for the first subject at b= 2000

s/mm^2. Figure 5(b)-5(d) shows the error plots from a superior slice of the brain with lots of fiber crossings and is far from regions affected by susceptibility and cardiac pulsation effects. Figure 5(f)-5(h) shows the error plots from an inferior slice of the brain that is subject to susceptibility and cardiac pulsation effects. The incoherent k-q scheme using the joint reconstruction is observed to perform better in both the slices compared to the other methods. The higher reconstruction errors observed in the inferior slice may be due to the presence of more gray matter regions in the inferior slice compared to the superior slices. The ODFs reconstructed using the various schemes from different regions of the brain are shown in Fig. 6. Figure 7 shows the results of the same experiments repeated on a second subject; the same trends of performance are observed here also. The optimal regularization parameters estimated from the first subject (reported in Table 1) were used in all the experiments performed on the second subject. This explains the slightly higher errors observed in the second dataset. Our experiments (not shown here) reveal that comparable errors can be obtained in the second dataset if the parameters were independently optimized. While selecting the parameters based on fully sampled ground truth is un-realistic in prospectively under sampled experiments, it may be possible to adapt the risk estimation based parameter optimization strategies (59, 60), which is beyond the scope of this work.

To verify the fact that the inaccurate noise modeling amplifies the error in the two-step schemes, ODFs are reconstructed from the fully sampled k-q data of the simulated data at three different noise levels. The reconstruction errors for the three cases are plotted in Fig. 2 in the supplementary materials. The plot shows that in the absence of noise, the two reconstruction schemes show similar performance. However, as the noise level increases, the reconstruction error gets higher in the two-step scheme compared to the joint scheme even at no acceleration.

The effect of a specific under-sampling pattern on the reconstruction scheme employed is studied in Fig. 8 and in Fig. 3 in the supplementary materials. It is observed from the plots that the joint reconstruction scheme employing incoherent under-sampling of the k-q space provides the best results. For the two-step optimization scheme, the k-only under-sampling scheme resulted in better angular estimates and peak detection; however, the NSSE error estimate does not exhibit a consistent pattern.

Table 2 lists the acquisition time of the various methods for different accelerations. It is evident from this table and the reconstruction errors that the proposed incoherent k-q scheme with joint reconstruction can efficiently accelerate the acquisition of simultaneously high spatial and angular resolution data.

Discussion

In spite of the obvious benefits of combining high angular and spatial resolution, prohibitively long ac-

quisition times have made such acquisitions challenging with conventional diffusion imaging techniques. In this work, we introduce a novel CS algorithm that is aimed at accelerating such acquisitions. The proposed scheme relies on improvements to the three key components of the CS scheme: model, acquisition scheme, and reconstruction. A complex partial volume model, which can represent the diffusion signal at all voxels and account for the phase of the diffusion signal is introduced. It enables the direct estimation of the coefficients from the measured k-space data. In addition to enabling flexible sampling of the k-q measurement space, this approach also enables to accurately account for noise statistics without compromising computational efficiency or convergence guarantees. Combined with the incoherent k-q under-sampling strategy, the above improvements result in a framework that enables to considerably reduce the scan time with minimal loss in accuracy. Specifically, our results show that accurate reconstruction with less than 5% reconstruction error is possible by using only 2-3 spatial interleaves per diffusion direction. This corresponds to an acquisition time of 6-8 mins for 17 slices at full FOV with a spatial resolution of $1mm^2$ in-plane.

Limitations and Future Work

A limitation of the validation in the current work is the absence of a true gold standard. Since there is no universally accepted gold-standard in HARDI, we have restricted our comparisons with fully sampled data, recovered using the same diffusion model. Thus it may overlook some of the confounds that cannot be modeled by the specific model. Hence, our results convey that the information that can be recovered from the fully sampled data using the diffusion model is still recoverable with sufficient accuracy from under-sampled data also.

Another drawback of the proposed scheme is its long reconstruction time (about 24 seconds per iteration) due to the large volume of data being used. Several improvements can be made to speed up the reconstruction on various fronts. For example, a significant fraction of reconstruction time is spent for motion compensation during every iteration. This time is proportional to the number of motion induced phase errors. By exploiting the redundancy in the motion-induced phase errors between shots, this step can be made faster (61). The reconstruction algorithm may also be made faster by replacing the conjugate gradient by faster methods like augmented Lagrangian (62) or split-Bregman methods (63). We plan to undertake these in our future work.

One possible enhancement to the current reconstruction framework is to further constrain the diffusion model. In the current implementation, the complex coefficients of the diffusion basis functions at specific voxel are assumed to be independent. However, at the current spatial scales, the coefficients in a specific voxel can be safely assumed to have the same phase. Since this reduces the number of degrees of freedom, this constraint may provide improved recovery. However, the resulting bi-linear optimization problem does

not have global convergence guarantees.

Although our model can capture the diffusion signal with reasonably good accuracy with the assumed diffusivity value, the fact that diffusivity is fixed is a weakness of our model. A more general model that can represent diffusion at all scales and is also sparse would be highly beneficial.

Since diffusion imaging is a signal-starved modality, SNR is a concern due to various reasons. In this context, a multi-shell sampling strategy may be worth exploring. By distributing the diffusion measurements onto different shells in q-space, the higher SNR of the lower shells and the higher resolving power of the higher shells may be combined (64, 65). Future work may extend the framework introduced here to multi-shell acquisitions.

In conclusion, we have proposed a novel under-sampling and reconstruction method to accelerate the acquisition of high angular and spatial resolution diffusion imaging. We showed that by under-sampling the combined k-q space jointly and incoherently and using a sparse model and a compressed sensing reconstruction, we can achieve high accelerations sufficient to enable high angular and spatial resolution diffusion imaging within a reasonable scan time.

Acknowledgements

The authors thank Prof Chunlei Liu and Prof Allen Song of Duke University for providing preliminary data for testing the algorithm.

Legends

Fig. 1: Illustration of various HARDI acquisition schemes using a multi-shot spiral k-space trajectory. (a) In a fully sampled acquisition, a large number of diffusion directions are collected at full-Nyquist sampling of the k-space points. The yellow dots on the black sphere represent the q-space points sampled. The different shots of the multi-shot k-space trajectory are represented using different colors. (b) Spatial under-sampling strategies (uniform k-only under-sampling) such as parallel imaging, under-sample the k-space of all the diffusion directions uniformly. All q-space points are sampled, however, the k-space of each q-space point is under-sampled; here only 4 shots are used and the same 4 shots are used for all q-space points. (c) Angular under-sampling schemes (q-only under-sampling) under-sample the q-space by collecting fewer diffusion directions. Only a subset of q-space points is sampled; here the k-space is fully sampled using all the 8 shots. (d) Hybrid k-q under-sampling schemes uniformly under-samples the k-space as well as the q-space independently. (e) The proposed incoherent k-q under-sampling scheme jointly and incoherently under-samples the combined k-q space. Here, each q-space point is sampled at different k-space locations using random k-space shots. Only 4 shots are used here; however instead of using the same 4 shots for all q-space points, they are sampled using different shots.

Fig. 2: Forward model showing the computation of $\mathcal{H}(\mathbf{V})$ for the q^{th} diffusion direction. The various symbols are defined as follows: $\mathbf{V}$ is the coefficient image, $\mathbf{a}_q$ is the q^{th} row of the diffusion model matrix $\mathbf{A}$, $\mathbf{s}_\mathrm{q}$ is the diffusion weighted image corresponding to the q^{th} diffusion direction, $\mathbf{P}_{q,i,j}$ are the composite sensitivity matrices corresponding to the q^{th} diffusion direction, i^{th} interleaf and j^{th} coil, $\mathbf{F}_{q,i}$ is the NUFFT matrix corresponding to the q^{th} diffusion direction and i^{th} interleaf and $\mathbf{y}_q$ is the k space measurement corresponding to the q^{th} diffusion direction.

Fig. 3: Error plots of reconstruction of in-vivo data at b =1200 $\mathrm{s/mm^2}$. (a) Normalized sum of square error of the ODFs, (b) average angular error, (c) rate of false peaks plotted against acceleration.

Fig. 4: In-vivo data at b=1200 $\mathrm{s/mm^2}$: (a) Boxed region marked shows the reference anatomical location in the brain for which the ODFs are plotted, (b) ODF of fully sampled data, (c) ODF reconstructed using incoherent k-q scheme at R=8, (d) ODF reconstructed using k-only scheme at R=8, (e) ODF reconstructed using q-only scheme at R=4. At acceleration of R=4, the angular resolution of the q-only scheme is compromised. The performance of k-only scheme is better than the q-only scheme. However, at R=8, k-only scheme fails to accurately represent the ODF profiles at many regions marked (arrows marked within in the three ovals). ODFs reconstructed using the incoherent k-q scheme resemble the fully sampled

data more closely.

Fig. 5: Plots of reconstruction errors from two different slices of subject 1 collected at b =2000 s/mm^2. Slice #1 is from the superior part of corpus callosum. Slice #2 is an inferior region that is prone to pulsatility and susceptibility effects. (b), (c) and (d) are the normalized sum of square error of the ODFs, average angular error, and rate of false peaks respectively for the slice shown in (a). (f),(g) and (h) are the normalized sum of square error of the ODFs, average angular error, and rate of false peaks respectively for the slice shown in (e).

Fig. 6: In-vivo data at b=2000 s/mm2 for subject 1 : (a) Boxed region marked shows the reference anatomical location in the brain for which the ODFs are plotted, (b) ODF of fully sampled data, (c) ODF reconstructed using incoherent k-q scheme at R=8, (d) ODF reconstructed using k-only scheme at R=8, (e) ODF reconstructed using q-only scheme at R=4. At acceleration of R=4, the angular resolution of the q-only scheme is severly compromised. The performance of k-only scheme is better than the q-only scheme. However, at R=8, k-only scheme fails to accurately represent the ODF profiles at many regions marked. ODFs reconstructed using the incoherent k-q scheme resembles the fully sampled data more closely.

Fig. 7: Plots of reconstruction errors from two different slices of subject 2 collected at b =2000 s/mm^2. Slice #1 is from the superior part of corpus callosum. Slice #2 is an inferior region that is prone to pulsatility and susceptibility effects. (b), (c) and (d) are the normalized sum of square error of the ODFs, average angular error, and rate of false peaks respectively for the slice shown in (a). (f),(g) and (h) are the normalized sum of square error of the ODFs, average angular error, and rate of false peaks respectively for the slice shown in (e).

Fig. 8: Plots of reconstruction errors from subject 1 and subject 2 collected at b =2000 s/mm^2 using various acquisition schemes. The joint optimization scheme was tested using incoherent k-q under-sampling (blue solid line) and uniform k-only under-sampling scheme(blue dotted line). Similarly, the two-step optimization scheme was tested using uniform k-only under-sampling scheme (red solid line) and incoherent k-q under-sampling scheme (red dotted line). Normalized ODF errors (b, f), average angular error (c, g) and rate of false peaks(d, h) are shown.

Table 1: Regularization parameters for various experiments.

Table 2: Acquisition time in minutes corresponding to various acceleration schemes.

References

1 P. J Basser, S. Pajevic, C. Pierpaoli, J. Duda, and A. Aldroubi. In vivo fiber tractography using DT-MRI data. *Magnetic Resonance in Medicine*, 44(4):625–632, 2000.

2 D. Le Bihan, E. Breton, D. Lallemand, P. Grenier, E. Cabanis, and M. Laval-Jeantet. MR imaging of intravoxel incoherent motions: application to diffusion and perfusion in neurologic disorders. *Radiology*, 161(2):401–7, 1986. ISSN 0033-8419.

3 E. O. Stejskal. Use of Spin Echoes in a Pulsed Magnetic-Field Gradient to Study Anisotropic, Restricted Diffusion and Flow. *The Journal of Chemical Physics*, 43(10):3597, 1965. ISSN 00219606.

4 L. Minati and W. P. Weglarz. Physical Foundations , Models , and Methods of Diffusion Magnetic Resonance Imaging of the Brain : A Review. *Concepts in Magnetic Resonance, Part A*, 30(5):278–307, 2007.

5 D. C Karampinos, A. T Van, W. C Olivero, J. G Georgiadis, and B. P Sutton. High-resolution diffusion tensor imaging of the human pons with a reduced field-of-view, multishot, variable-density, spiral acquisition at 3 T. *Magnetic Resonance in Medicine*, 62(4):1007–1016, 2009.

6 A. L Alexander, K. M Hasan, M. Lazar, J. S Tsuruda, and D. L Parker. Analysis of partial volume effects in diffusion-tensor MRI. *Magnetic Resonance in Medicine*, 45(5):770–780, 2001.

7 H. Oouchi, K. Yamada, K. Sakai, O. Kizu, T. Kubota, H. Ito, and T. Nishimura. Diffusion anisotropy measurement of brain white matter is affected by voxel size: underestimation occurs in areas with crossing fibers. *American Journal Of Neuroradiology*, 28(6):1102–1106, 2007.

8 M. Kim, I. Ronen, K. Ugurbil, and D.-S. Kim. Spatial resolution dependence of DTI tractography in human occipito-callosal region. *NeuroImage*, 32(3):1243–1249, 2006.

9 L. Zhan, A. D Leow, N. Jahanshad, M.-C. Chiang, M. Barysheva, A. D Lee, A. W Toga, K. L McMahon, G. I. De Zubicaray, M. J Wright, and P. M Thompson. How does angular resolution affect diffusion imaging measures? *NeuroImage*, 49(2):1357–1371, 2010.

10 J. E Sarlls and C. Pierpaoli. Diffusion-weighted radial fast spin-echo for high-resolution diffusion tensor imaging at 3T. *Magnetic Resonance in Medicine*, 60(2):270–276, 2008.

11 Y. Ye, Y. Zhuo, J. An, and X. J. Zhou. A Navigated non-CPMG Turbo Spin Echo Pulse Sequence for High Resolution Diffusion Imaging. In *Proc Intl Soc Mag Reson Med*, volume 18, page 759, 2008.

12 D. H. J. Poot, B. Jeurissen, Y. Bastiaensen, J. Veraart, W. Van Hecke, P. M. Parizel, and J. Sijbers. Super-resolution for multislice diffusion tensor imaging. *Magnetic Resonance in Medicine*, 69(1):103–13, 2013. ISSN 07403194.

13 Z. Ding, J. C. Gore, and A. W. Anderson. Reduction of noise in diffusion tensor images using anisotropic smoothing. *Magnetic Resonance in Medicine*, 53(2):485–490, 2005.

14 J. P Haldar, V. J Wedeen, M. Nezamzadeh, G. Dai, N. Schuff, and Z.-P. Liang. Improved diffusion imaging through SNR-enhancing joint reconstruction. *Magnetic Resonance in Medicine*, 69:277–289, 2013.

15 C. Liu, R. Bammer, and M. E Moseley. High resolution multi-shot SENSE DTI using self-navigated interleaved spirals (SNAILS). *Magnetic Resonance in Medicine*, 13(1), 2005.

16 T. Jaermann, K. P Pruessmann, A. Valavanis, S. Kollias, and P. Boesiger. Ultra-high Resolution SENSE-DTI at 3 Tesla. *Magnetic Resonance in Medicine*, 11:2003, 2003.

17 S. Rieseberg, K.-D. Merboldt, M. Küntzel, and J. Frahm. Diffusion tensor imaging using partial Fourier STEAM MRI with projection onto convex subsets reconstruction. *Magnetic Resonance in Medicine*, 54(2):486–490, 2005.

18 S. J. Holdsworth, S. Skare, R. D. Newbould, and R. Bammer. Robust GRAPPA-accelerated diffusion-weighted readout-segmented (RS)-EPI. *Magnetic resonance in medicine*, 62(6):1629–40, 2009. ISSN 1522-2594.

19 R. Bammer, S. L. Keeling, M. Augustin, K. P. Pruessmann, R. Wolf, R. Stollberger, H. P. Hartung, and F. Fazekas. Improved diffusion-weighted single-shot echo-planar imaging (EPI) in stroke using sensitivity encoding (SENSE). *Magnetic Resonance in Medicine*, 46(3):548–554, 2001.

20 A. B. Kerr, J. M. Pauly, and D. G. Nishimura. Partial k- Space Acquisition for Real- Time MR Imaging. In *Proc Intl Soc Mag Reson Med*, volume 10, page 1945, 1998.

21 C. Lin, W. I. Tseng, J. Weng, V. J. Wedeen, and J. Chen. Reduced Encoding of Diffusion Spectrum Imaging with Cross-term Correction. In *Proc Intl Soc Mag Reson Med*, volume 21, page 2141, 2003.

22 A. T. Van, R. O. Halloran, S. Holdsworth, and R. Bammer. Rapid Diffusion Spectrum Imaging with Partial q-Space Encoding. In *Proc Intl Soc Mag Reson Med*, volume 19, page 9784, 2011.

23 B. A. Landman, H. Wan, J. A. Bogovic, P.-L. Bazin, and J. L. Prince. Resolution of Crossing Fibers with Constrained Compressed Sensing using Traditional Diffusion Tensor MRI. *Proc - Society of Photo-Optical Instrumentation Engineers*, 7623(8):76231H, 2010. ISSN 1018-4732.

24 S. Merlet and R. Deriche. Compressed Sensing for Accelerated EAP Recovery in Diffusion MRI. *Imaging*, pages 14–25, 2010.

25 O. Michailovich, Y. Rathi, and S. Dolui. Spatially regularized compressed sensing for high angular resolution diffusion imaging. *IEEE Transactions on Medical Imaging*, 30(5):1100–15, 2011. ISSN 1558-0062.

26 M. I. Menzel, E. T. Tan, K. Khare, J. I. Sperl, K. F. King, X. Tao, C. J. Hardy, and L. Marinelli. Accelerated diffusion spectrum imaging in the human brain using compressed sensing. *Magnetic Resonance in Medicine*, 66 (5):1226–1233., 2011. ISSN 07403194.

27 S. Merlet, J. Cheng, A. Ghosh, and R. Deriche. Spherical Polar Fourier EAP and ODF Reconstruction via Compressed Sensing in Diffusion MRI. *ISBI*, 2011.

28 B. Bilgic, K. Setsompop, J. Cohen-Adad, V. Wedeen, L. L. Wald, and E. Adalsteinsson. Accelerated diffusion spectrum imaging with compressed sensing using adaptive dictionaries. In *Medical Image Computing and Computer-Assisted Intervention*, volume 15, pages 1–9, 2012.

29 C. L. Welsh, E. W. Hsu, and E. V. DiBella. Model-Based Reconstruction of Undersampled DTI Data. *Magnetic Resonance in Medicine*, 70:429–440, 2013.

30 Y. Wu, Y.-j. Zhu, Q.-y. Tang, C. Zou, W. Liu, R.-b. Dai, X. Liu, E. X. Wu, L. Ying, and D. Liang. Accelerated MR diffusion tensor imaging using distributed compressed sensing. *Magnetic Resonance in Medicine*, 000:1–10, 2013. ISSN 15222594.

31 E. Candes, J. Romberg, and T. Tao. Robust uncertainty principles: exact signal reconstruction from highly incomplete frequency information. *IEEE Transactions on Information Theory*, 52(2):489–509, 2006. ISSN 0018-9448.

32 D. Donoho. Compressed Sensing. *IEEE Transactions on Information Theory*, 52(4):1289 – 1306, 2006.

33 M. Lustig, D. Donoho, J. Santos, and J. Pauly. Compressed Sensing MRI. *IEEE Signal Processing Magazine*, 25 (2):72–82, 2008. ISSN 1053-5888.

34 A. Raj, C. Hess, and P. Mukherjee. Spatial HARDI: improved visualization of complex white matter architecture with Bayesian spatial regularization. *NeuroImage*, 54(1):396–409, 2011. ISSN 1095-9572.

35 B. Jeurissen, A. Leemans, J.-D. Tournier, D. K. Jones, and J. Sijbers. Estimating the number of fiber orientations in diffusion MRI voxels : a constrained spherical deconvolution study. In *Proc Intl Soc Mag Reson Med*, volume 18, 2010.

36 T. E. J Behrens, M. W Woolrich, M. Jenkinson, H. Johansen-Berg, R. G Nunes, S. Clare, P. M Matthews, J. M Brady, and S. M Smith. Characterization and propagation of uncertainty in diffusion-weighted MR imaging. *Magnetic Resonance in Medicine*, 50(5):1077–1088, 2003.

37 T. Hosey, G. Williams, and R. Ansorge. Inference of multiple fiber orientations in high angular resolution diffusion imaging. *Magnetic Resonance in Medicine*, 54(6):1480–1489, 2005.

38 Y. Wang, Q. Wang, J. P. Haldar, F. C. Yeh, M. Xie, P. Sun, T. W. Tu, K. Trinkaus, R. S. Klein, A. H. Cross, and S. K. Song. Quantification of increased cellularity during inflammatory demyelination. *Brain*, 134(12): 3587–3598, 2011. ISSN 00068950.

39 S. Dolui, A. Kuurstra, and O. V. Michailovich. Rician Compressed Sensing for Fast and Stable Signal Reconstruction in Diffusion MRI. In *SPIE Medical Imaging*, pages 83144Q–10, 2012.

40 F. Lam, S. D. Babacan, J. P. Haldar, N. Schuff, and Z.-P. Liang. Denoising diffusion-weighted MR magnitude image sequences using low rank and edge constraints. In *IEEE International Symposium on Biomedical Imaging (ISBI)*, pages 1401–1404, 2012. ISBN 978-1-4577-1858-8.

41 S. Basu, T. Fletcher, and R. Whitaker. Rician noise removal in diffusion tensor MRI. In *Medical image computing and computer-assisted intervention : MICCAI*, volume 9, pages 117–25, 2006.

42 C. Liu, R. Bammer, D.-H. Kim, and M. E. Moseley. Self-navigated interleaved spiral (SNAILS): application to high-resolution diffusion tensor imaging. *Magnetic resonance in medicine*, 52(6):1388–96, 2004. ISSN 0740-3194.

43 M. Mani, M. Jacob, A. Guidon, C. Liu, A. Song, V. Magnotta, and J. Zhong. Acceleration of high angular and spatial resolution diffusion imaging using compressed sensing. In *IEEE International Symposium on Biomedical Imaging (ISBI)*, pages 326–329, 2012. ISBN 978-1-4577-1858-8.

44 T. E. J. Behrens, H. J. Berg, S. Jbabdi, M. F. S. Rushworth, and M. W. Woolrich. Probabilistic diffusion tractography with multiple fibre orientations: What can we gain? *NeuroImage*, 34(1):144–55, 2007. ISSN 1053-8119.

45 C. Pierpaoli, P. Jezzard, P. Basser, A. Barnett, and G. Chiro. Diffusion Tensor MR Imaging of the Human Brain. *Radiology*, 201:637–648, 1996.

46 I. Aganj, C. Lenglet, G. Sapiro, E. Yacoub, K. Ugurbil, and N. Harel. Reconstruction of the orientation distribution function in single- and multiple-shell q-ball imaging within constant solid angle. *Magnetic Resonance in Medicine*, 64(2):554–66, 2010. ISSN 1522-2594.

47 C. Liu, M. E. Moseley, and R. Bammer. Simultaneous phase correction and SENSE reconstruction for navigated multi-shot DWI with non-cartesian k-space sampling. *Magnetic resonance in medicine*, 54(6):1412–22, 2005. ISSN 0740-3194.

48 M. Uecker, A. Karaus, and J. Frahm. Inverse reconstruction method for segmented multishot diffusion-weighted MRI with multiple coils. *Magnetic Resonance in Medicine*, 62(5):1342–1348, 2009.

49 R. Gribonval and M. Nielsen. Sparse representations in unions of bases. *IEEE Transactions on Information Theory*, 49(12):3320–3325, 2003. ISSN 0018-9448.

50 D. L. Donoho. Optimally sparse representation in general (nonorthogonal) dictionaries via ell 1 minimization. *Proceedings of the National Academy of Sciences*, 100(5):2197–2202, 2003. ISSN 00278424.

51 I. Daubechies, R. DeVore, M. Fornasier, and C. S. Güntürk. Iteratively reweighted least squares minimization for sparse recovery. *Communications on Pure and Applied Mathematics*, 63(1):1–38, January 2010. ISSN 00103640.

52 N. Bissantz, L. Dümbgen, A. Munk, and B. Stratmann. Convergence Analysis of Generalized Iteratively Reweighted Least Squares Algorithms on Convex Function Spaces. *SIAM Journal on Optimization*, 19(4): 1828–1845, January 2009. ISSN 1052-6234.

53 B. Wohlberg and P. Rodriguez. An Iteratively Reweighted Norm Algorithm for Minimization of Total Variation Functionals. *IEEE Signal Processing Letters*, 14(12):948–951, 2007. ISSN 1070-9908.

54 M. Jacob. Efficient NUFFT algorithm for non-Cartesian MRI reconstruction. In *2009 IEEE International Symposium on Biomedical Imaging: From Nano to Macro*, pages 117–120. IEEE, 2009. ISBN 978-1-4244-3931-7.

55 S. Ramani, T. Blu, and M. Unser. Monte-Carlo sure: a black-box optimization of regularization parameters for general denoising algorithms. *IEEE Transactions on Image Processing*, 17(9):1540–1554, 2008.

56 O. Scherzer. The use of Morozov's discrepancy principle for Tikhonov regularization for solving nonlinear ill-posed problems. *Computing*, 51(1):45–60, 1993. ISSN 0010-485X.

57 M. Belge, M. E. Kilmer, and E. L. Miller. Efficient Determination of Multiple Regularization Parameters in a Generalized L-curve Framework. *Inverse Problems*, 18(4):1161, 2002.

58 S. Bhave, R. Eslami, and M. Jacob. Sparse spectral deconvolution algorithm for noncartesian MR spectroscopic imaging. *Magnetic Resonance in Medicine*, 2013. ISSN 1522-2594.

59 S. Ramani, Z. Liu, J. Rosen, J. Nielsen, and J. Fessler. Regularization Parameter Selection for Nonlinear Iterative Image Restoration and MRI Reconstruction Using GCV and SURE-Based Methods. *IEEE Transactions on Image Processing*, 21(8):1–14, 2012. ISSN 19410042.

60 E. J. Candes, C. A. Sing-Long, and J. D. Trzasko. Unbiased Risk Estimates for Singular Value Thresholding and Spectral Estimators. *IEEE Transactions on Signal Processing*, 61(19):4643–4657, October 2013. ISSN 1053-587X.

61 M. Mani, M. Jacob, A. Guidon, V. Magnotta, and J. Zhong. Accelerating non-Cartesian sense for large coil arrays: Application to motion compensation in multishot DWI. In *IEEE International Symposium on Biomedical Imaging (ISBI)*, pages 406–409, 2012. ISBN 978-1-4577-1858-8.

62 M. V Afonso, J. M Bioucas-Dias, and M. A. T Figueiredo. An Augmented Lagrangian Approach to the Constrained Optimization Formulation of Imaging Inverse Problems. *IEEE Transactions on Image Processing*, 20(3):681–695, 2011.

63 W. Yin, S. Osher, D. Goldfarb, and J. Darbon. Bregman Iterative Algorithms for l1-Minimization with Applications to Compressed Sensing. *SIAM J Imaging Sciences*, 1(1):143–168, 2008.

64 M. H. Khachaturian, J. J. Wisco, and D. S. Tuch. Boosting the sampling efficiency of q-Ball imaging using multiple wavevector fusion. *Magnetic Resonance in Medicine*, 57(2):289–296, 2007.

65 Y.-C. Wu, A. S. Field, and A. L. Alexander. Computation of Diffusion Function Measures in -Space Using Magnetic Resonance Hybrid Diffusion Imaging. *IEEE Transactions on Medical Imaging*, 27(6):858–865, 2008.

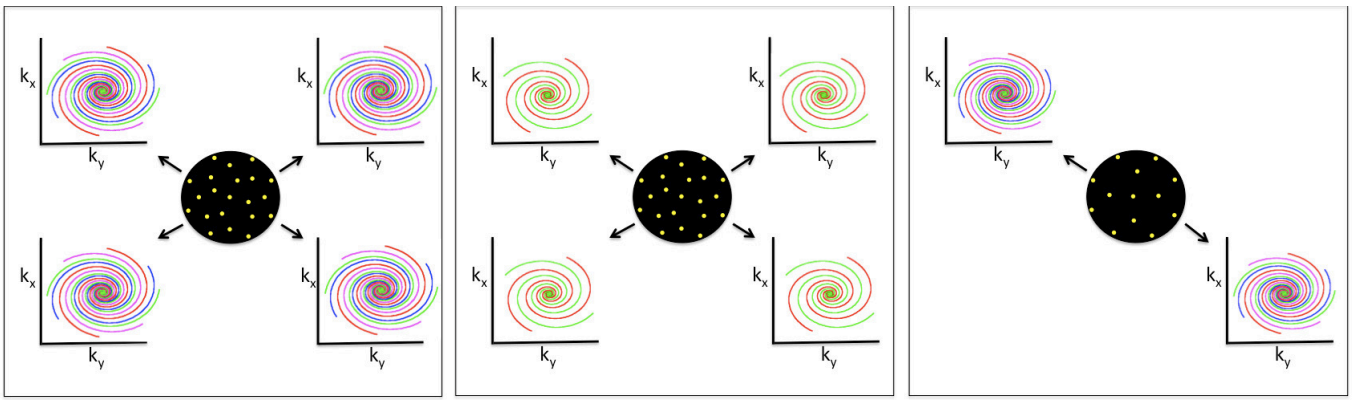

(a) fully sampled acquisition (b) uniform k-only under-sampling (c) uniform q-only under-sampling

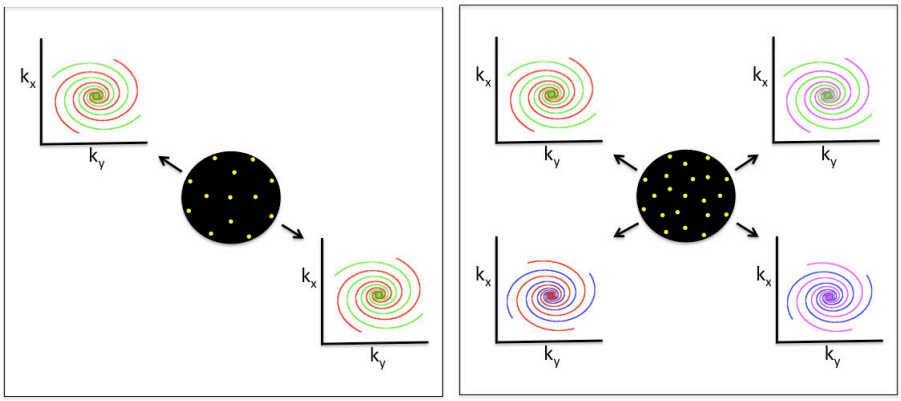

(d) hybrid k-q under-sampling (e) incoherent k-q under-sampling

Figure 1: Illustration of various HARDI acquisition schemes using a multi-shot spiral k-space trajectory. (a) In a fully sampled acquisition, a large number of diffusion directions are collected at full-Nyquist sampling of the k-space points. The yellow dots on the black sphere represent the q-space points sampled. The different shots of the multi-shot k-space trajectory are represented using different colors. (b) Spatial under-sampling strategies (uniform k-only under-sampling) such as parallel imaging, under-sample the k-space of all the diffusion directions uniformly. All q-space points are sampled, however, the k-space of each q-space point is under-sampled; here only 4 shots are used and the same 4 shots are used for all q-space points. (c) Angular under-sampling schemes (q-only under-sampling) under-sample the q-space by collecting fewer diffusion directions. Only a subset of q-space points is sampled; here the k-space is fully sampled using all the 8 shots. (d) Hybrid k-q under-sampling schemes uniformly under-samples the k-space as well as the q-space independently. (e) The proposed incoherent k-q under-sampling scheme jointly and incoherently under-samples the combined k-q space. Here, each q-space point is sampled at different k-space locations using random k-space shots. Only 4 shots are used here; however instead of using the same 4 shots for all q-space points, they are sampled using different shots.

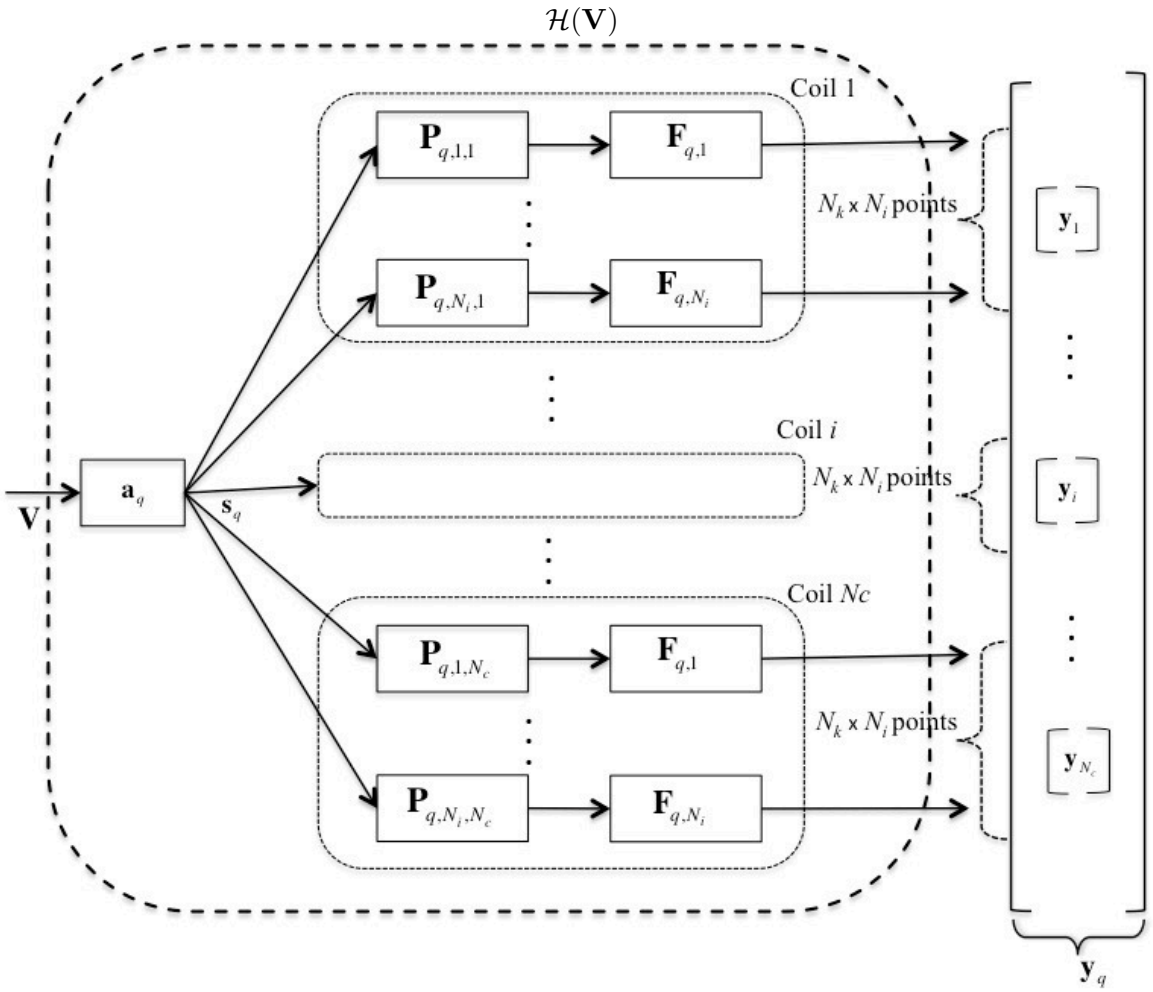

(a)

Figure 2: Forward model showing the computation of $\mathcal{H}(\mathbf{V})$ for the q^{th} diffusion direction. The various symbols are defined as follows: $\mathbf{V}$ is the coefficient image, $\mathbf{a}_q$ is the q^{th} row of the diffusion model matrix $\mathbf{A}$, $\mathbf{s}_\mathrm{q}$ is the diffusion weighted image corresponding to the q^{th} diffusion direction, $\mathbf{P}_{q,i,j}$ are the composite sensitivity matrices corresponding to the q^{th} diffusion direction, i^{th} interleaf and j^{th} coil, $\mathbf{F}_{q,i}$ is the NUFFT matrix corresponding to the q^{th} diffusion direction and i^{th} interleaf and $\mathbf{y}_q$ is the k space measurement corresponding to the q^{th} diffusion direction.

Table 1: Regularization parameters for various experiments

method	$\beta's$	R=2	R=4	R=8	R=11
$b = 1200s/mm^2$					
incoherent k-q	β_1	5e-06	1e-05	1e-05	1e-04
	β_2	5e-04	5e-04	1e-04	1e-04
k-only	β_1	1e-04	1e-04	1e-04	1e-04
	β_2	5e-05	5e-05	5e-05	5e-05
hybrid k-q;32 dir	β_1		1e-04	1e-04	
	β_2		2e-05	2e-05	
hybrid k-q;16dir	β_1			1e-04	
	β_2			2e-05	
q-only	β_1	1e-03	1e-03	1e-04	
	β_2	5e-06	5e-06	5e-06	
$b = 2000s/mm^2$					
incoherent k-q	β_1	5e-06	5e-06	5e-06	1e-06
	β_2	5e-03	1e-03	1e-03	1e-03
k-only	β_1	1e-04	1e-04	1e-04	1e-04
	β_2	1e-04	1e-04	1e-04	1e-04
hybrid k-q;32 dir	β_1		1e-03	5e-04	
	β_2		1e-04	1e-04	
hybrid k-q;16dir	β_1			5e-03	
	β_2			1e-04	
q-only	β_1	5e-03	5e-03	1e-02	
	β_2	1e-04	1e-04	1e-04	

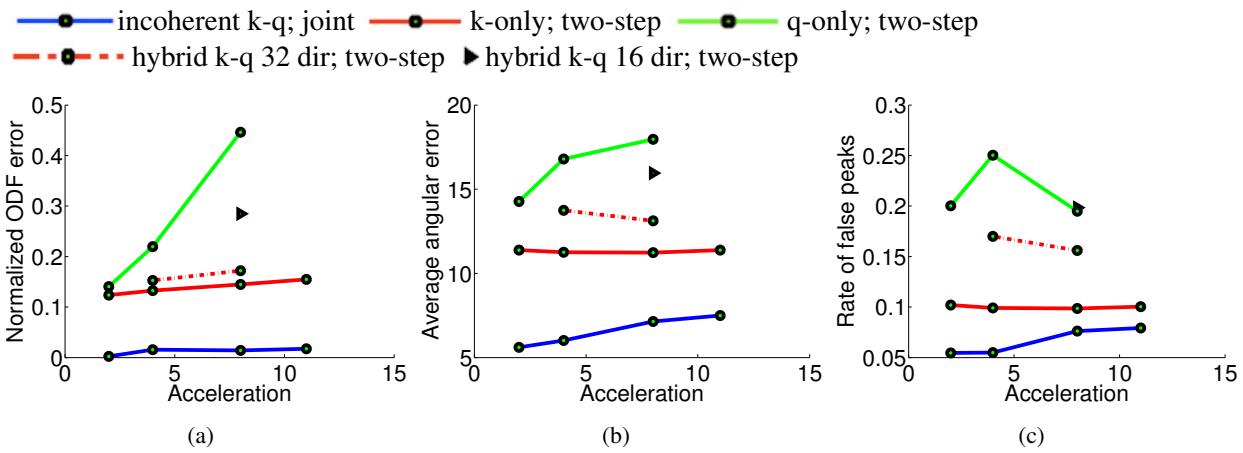

Figure 3: Error plots of reconstruction of in-vivo data at b =1200 s/mm^2. (a) Normalized sum of square error of the ODFs, (b) average angular error, (c) rate of false peaks plotted against acceleration.

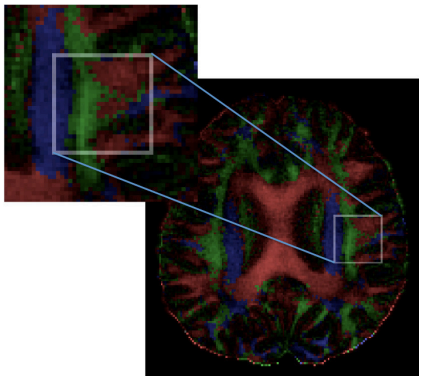

(a) Region of interest

Figure 4: In-vivo data at b=1200 s/mm^2 : (a) Boxed region marked shows the reference anatomical location in the brain for which the ODFs are plotted, (b) ODF of fully sampled data, (c) ODF reconstructed using incoherent k-q scheme at R=8, (d) ODF reconstructed using k-only scheme at R=8, (e) ODF reconstructed using q-only scheme at R=4. At acceleration of R=4, the angular resolution of the q-only scheme is compromised. The performance of k-only scheme is better than the q-only scheme. However, at R=8, k-only scheme fails to accurately represent the ODF profiles at many regions marked (arrows marked within in the three ovals). ODFs reconstructed using the incoherent k-q scheme resemble the fully sampled data more closely.

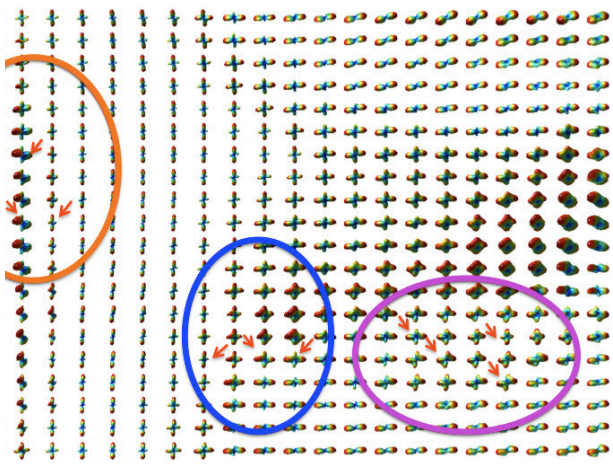

(b) reference ODF

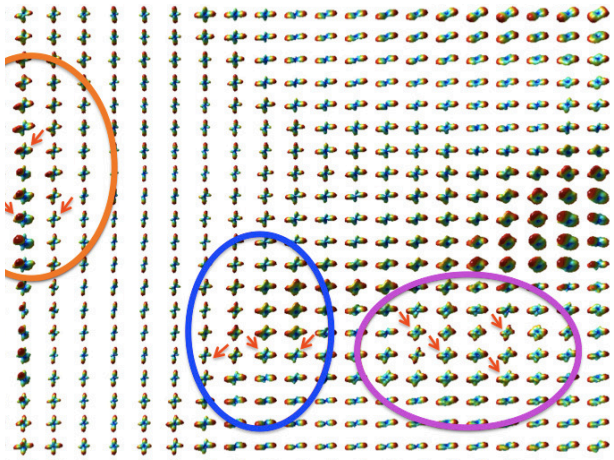

(c) incoherent k-q scheme; R=8

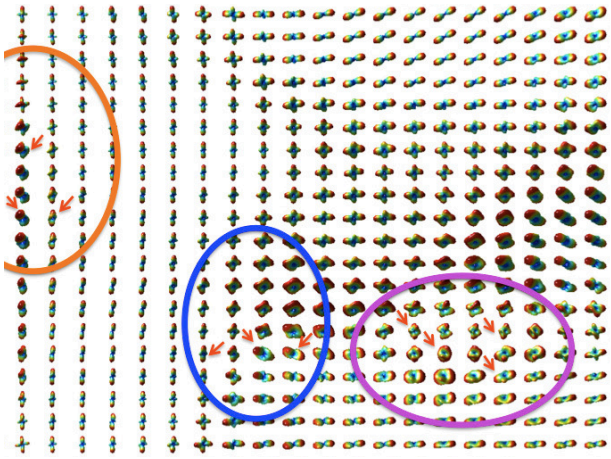

(d) k-only scheme; R=8

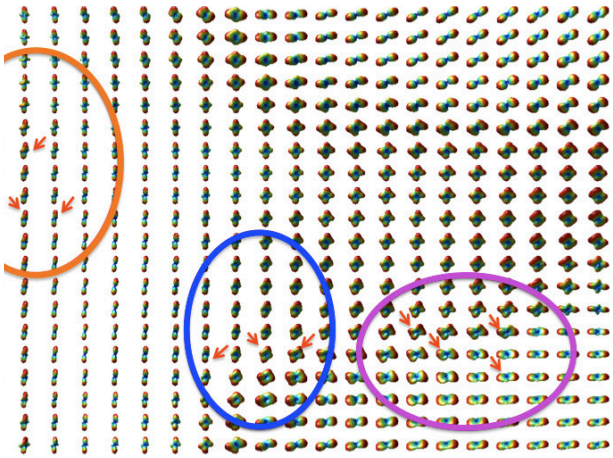

(e) q-only scheme; R=4

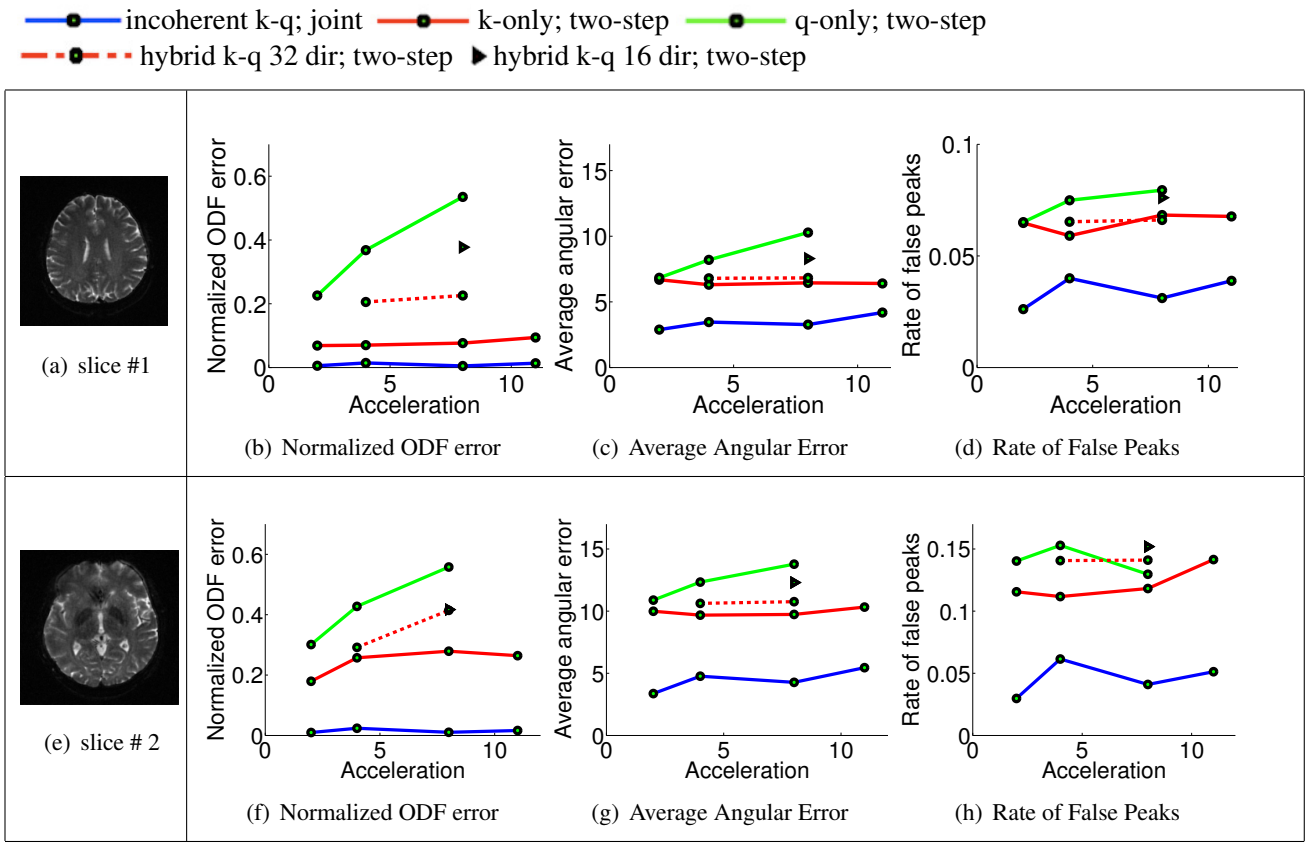

Figure 5: Plots of reconstruction errors from two different slices of subject 1 collected at b =2000 s/mm^2. Slice #1 is from the superior part of corpus callosum. Slice #2 is an inferior region that is prone to pulsatility and susceptibility effects. (b), (c) and (d) are the normalized sum of square error of the ODFs, average angular error, and rate of false peaks respectively for the slice shown in (a). (f), (g) and (h) are the normalized sum of square error of the ODFs, average angular error, and rate of false peaks respectively for the slice shown in (e).

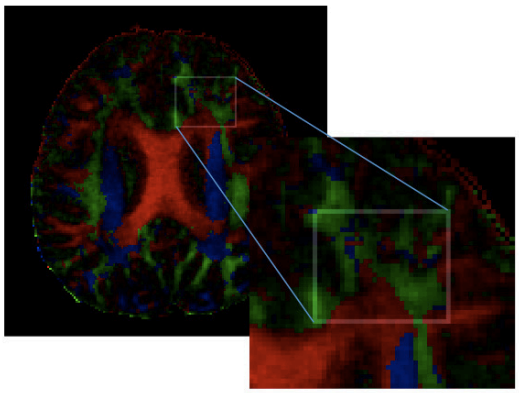

(a) Region of interest

Figure 6: In-vivo data at b=2000 s/mm^2 for subject 1 : (a) Boxed region marked shows the reference anatomical location in the brain for which the ODFs are plotted, (b) ODF of fully sampled data, (c) ODF reconstructed using incoherent k-q scheme at R=8, (d) ODF reconstructed using k-only scheme at R=8, (e) ODF reconstructed using q-only scheme at R=4. At acceleration of R=4, the angular resolution of the q-only scheme is severly compromised. The performance of k-only scheme is better than the q-only scheme. However, at R=8, k-only scheme fails to accurately represent the ODF profiles at many regions marked. ODFs reconstructed using the incoherent k-q scheme resembles the fully sampled data more closely.

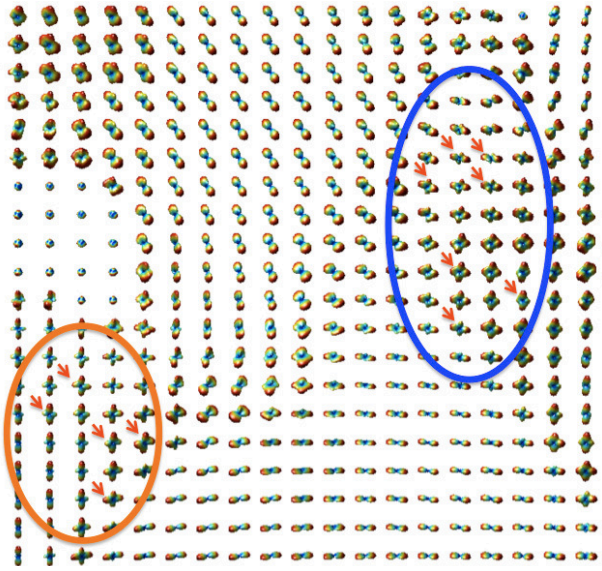

(b) reference ODF

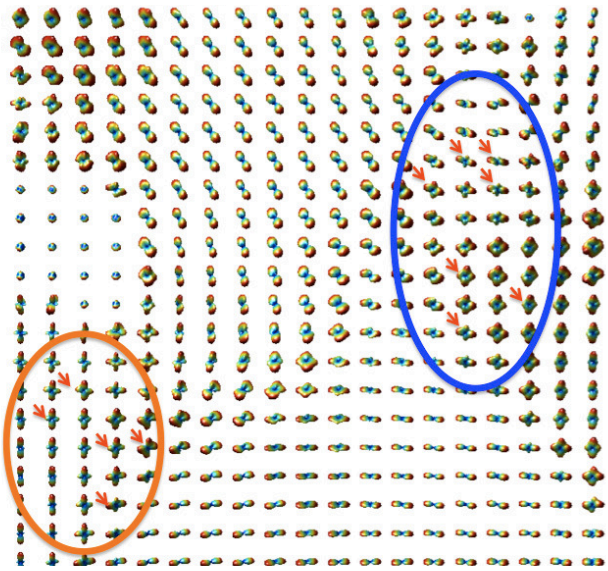

(c) incoherent k-q; R=8

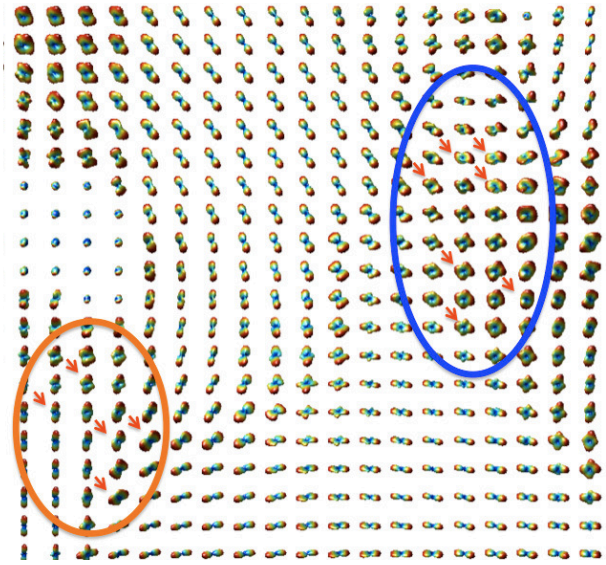

(d) k-only; R=8

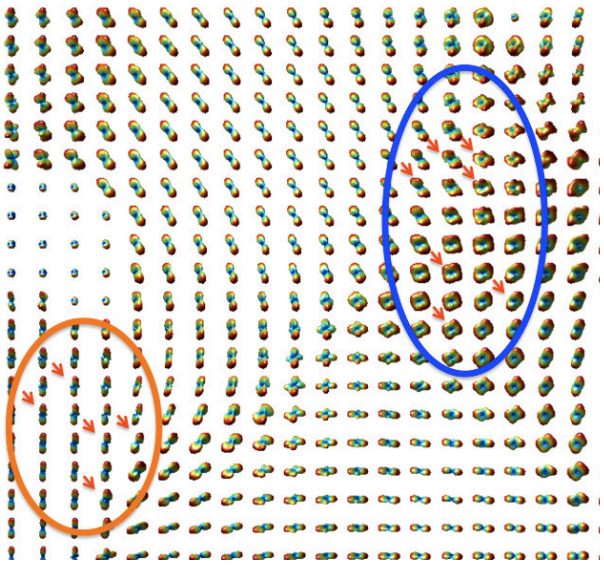

(e) q-only;R=4

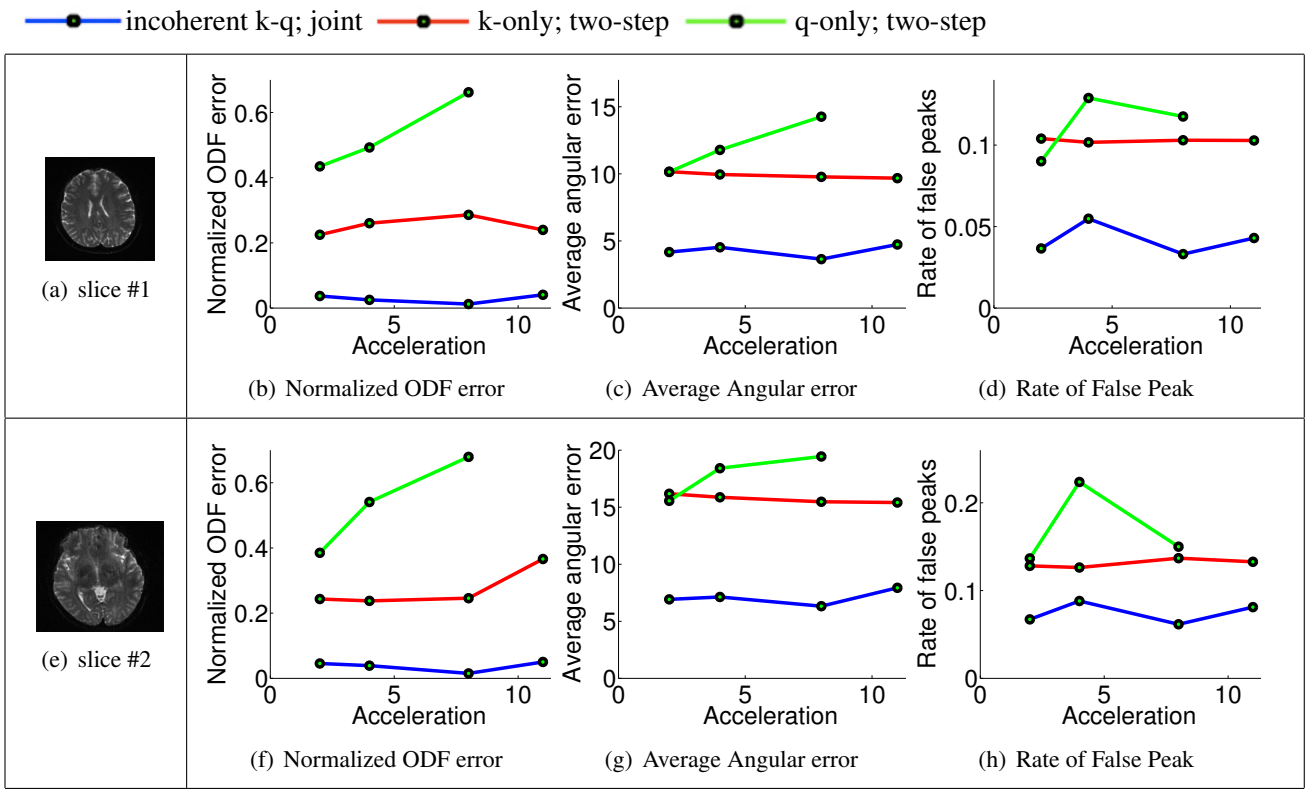

Figure 7: Plots of reconstruction errors from two different slices of subject 2 collected at b =2000 s/mm^2. Slice #1 is from the superior part of corpus callosum. Slice #2 is an inferior region that is prone to pulsatility and susceptibility effects. (b), (c) and (d) are the normalized sum of square error of the ODFs, average angular error, and rate of false peaks respectively for the slice shown in (a). (f), (g) and (h) are the normalized sum of square error of the ODFs, average angular error, and rate of false peaks respectively for the slice shown in (e).

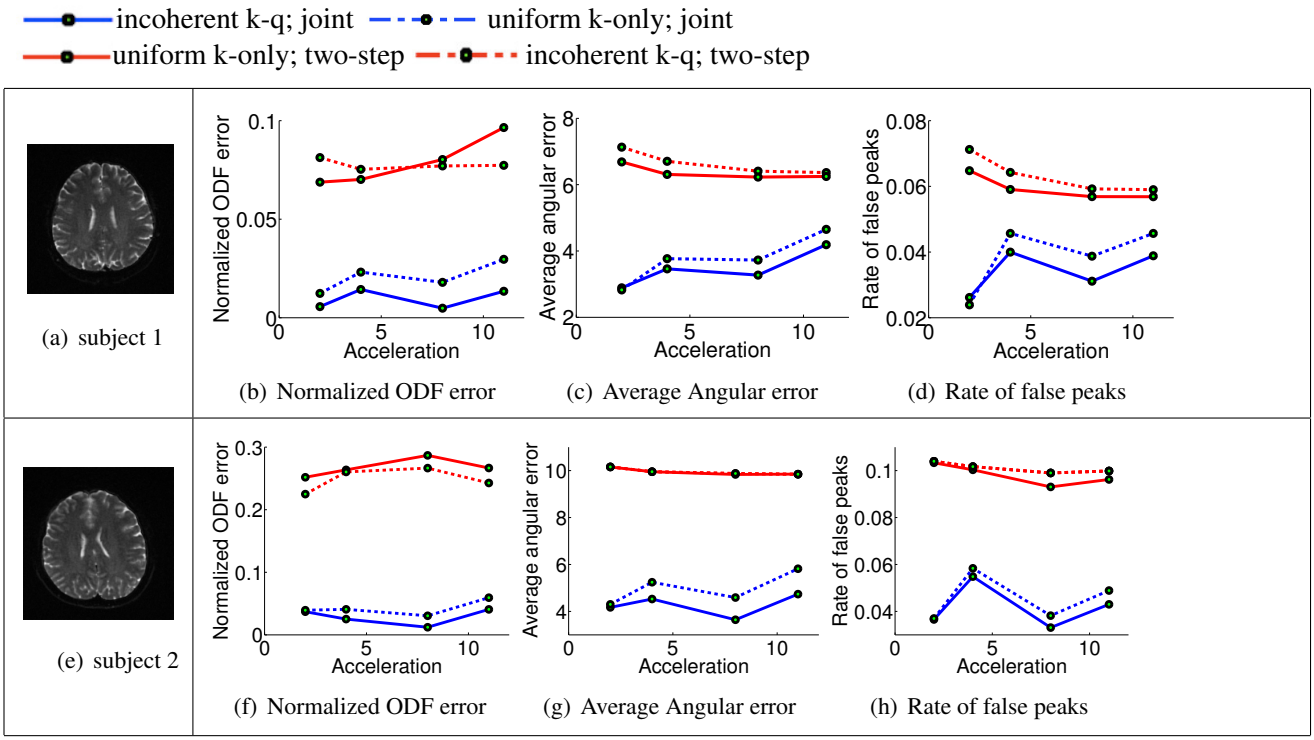

Figure 8: Plots of reconstruction errors from subject 1 and subject 2 collected at b =2000 s/mm^2 using various acquisition schemes. The joint optimization scheme was tested using incoherent k-q under-sampling (blue solid line) and uniform k-only under-sampling scheme (blue dotted line). Similarly, the two-step optimization scheme was tested using uniform k-only under-sampling scheme (red solid line) and incoherent k-q under-sampling scheme (red dotted line). Normalized ODF errors (b, f), average angular error (c, g) and rate of false peaks(d, h) are shown.

Table 2: Acquisition time in minutes corresponding to various acceleration schemes.

Method	R=1	R=2	R=4	R=8	R=11
incoherent k-q	60	30	16.25	8	5.3
k-only	60	30	16.25	8	5.3
hybrid k-q; 32 dir	60		15.58	8.9	
hybrid k-q; 16 dir	60			8.25	
q-only	60	30	15.58	8.25	6.41

Supplementary material

Simulated data and experiements

We create a numerical simulation data from an in-vivo human dataset that was collected at a b-value of 1200 s/mm^2 with 60 diffusion directions. This data was collected using a variable density spiral trajectory with 22 interleaves at a spatial resolution of 1mm x 1mm x 1.5 mm with an 8 channel head coil. The diffusion images corresponding to the 60 diffusion directions were reconstructed using a SENSE reconstruction and motion corrected. Using the model matrix $\mathbf{A}$ that was created for the 60 diffusion directions, the dominant diffusion directions in each voxel of the in-vivo data were found using a matching pursuit algorithm in a greedy fashion (1). Diffusion components were fit to the signal in each voxel until the error between the simulated signal and the real signal were below a fixed value. Thus, the number of diffusion directions in each voxel varied and were determined automatically based on the residual error after fitting. Once the diffusion basis functions were obtained this way, the simulated diffusion weighted images was obtained using the forward model in Eq. [5]. Then, k-space data corresponding to each channel and spiral interleaf were computed for 60 diffusion directions using Eq. [8] without the motion error. Complex Gaussian noise was added to the k-space predictions of the dataset such that the noise variance of the k-space data for each channel and each diffusion direction matched that of the in-vivo data from which it is created. Figure 1 shows the ODF of simulated data for a small region of the brain.

To study the effect of noise on the joint and two-step reconstruction schemes, we performed the following experiment on the simulated data. ODFs were reconstructed using the joint k-q scheme and two-step scheme from the fully sampled data at three noise levels: (i) no noise was added, (ii) complex Gaussian noise with half the noise variance as that of the in-vivo k-space data was added, and (iii) complex Gaussian noise with full noise variance as that of the in-vivo k-space data was added. The reconstruction errors for these three cases were computed and are plotted in Fig. 2. The plot shows that in the absence of noise, the two schemes shows similar performance. However, as the noise level increase, the reconstruction error is higher in the two-step scheme compared to the joint scheme even at no acceleration.

The effect of the various under-sampling patterns on the reconstruction scheme employed were studied on the simulated data. Reconstructions were performed under four different settings. The simulated k-space data was under-sampled using incoherent k-q under-sampling and reconstructed using (i) the joint reconstruction scheme and (ii) the two-step reconstruction scheme. Similarly, the k-q data was under-sampled using the uniform k-only under-sampling scheme and reconstructed using (i) the joint reconstruction scheme and (ii) the two-step reconstruction scheme. The results of the these experiments are plotted in Fig. 3. It is observed from the plots that the joint reconstruction scheme employing incoherent under-sampling of the

k-q space provides the best results.

Legends

Fig 1: Numerical data simulated from an in-vivo brain region : (a) RGB map of the in-vivo brain data from which the simulated data was created, (b) Ground truth ODF (without noise) corresponding to the boxed region in (a).

Fig 2: Effect of noise on reconstruction. The blue graph represents the joint reconstruction and the red graph represents the two-step magnitude based scheme. In the absence of noise, the two schemes shows similar performance. As noise level increases, the error in the two-step magnitude-based scheme increases because of the inaccurate noise modeling.

Fig 3: Effect of under-sampling pattern on reconstruction. The blue graph represents the joint reconstruction scheme that reconstructs the ODF directly from k-q data. The blue solid line represents the plots using the incoherent k-q under-sampling pattern and the blue dotted line represents plots using the uniform k-only under-sampling. The red graph represents the scheme that reconstructs the ODF using the two-step scheme. The red solid line represents the plots using the uniform k-only under-sampling pattern and the red dotted line represents plots using the incoherent k-q under-sampling pattern.

References

1 S. Mallat. Matching pursuits with time-frequency dictionaries. *IEEE Transactions on Signal Processing*, 41(12): 3397–3415, 1993. ISSN 1053587X.

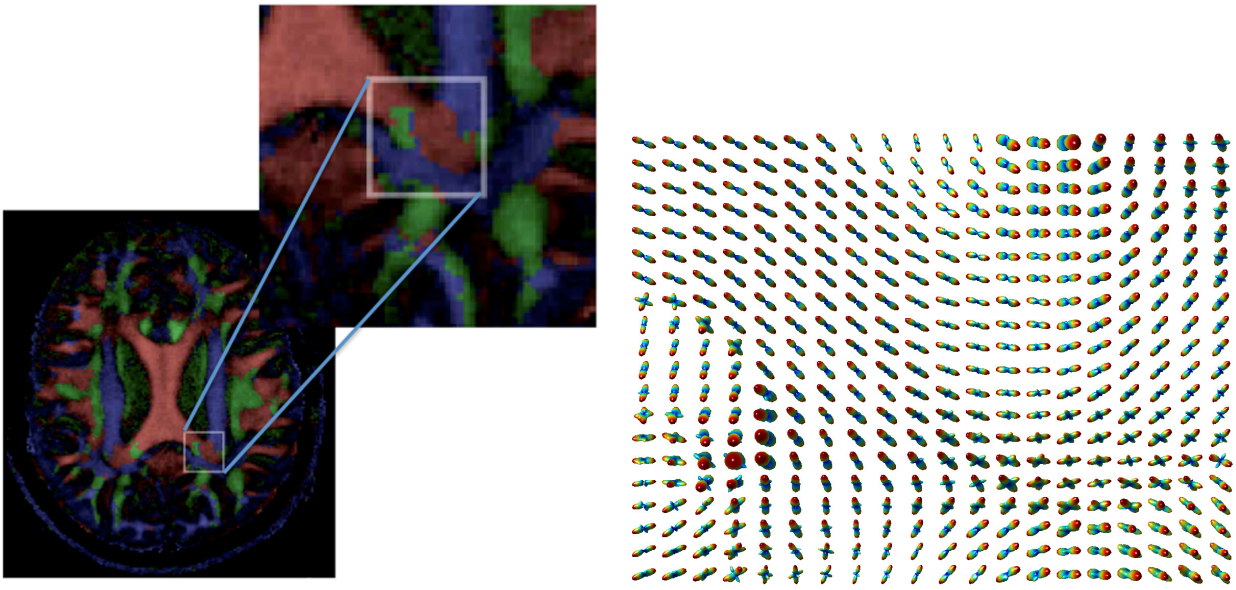

(a) (b)

Figure 1: Numerical data simulated from an in-vivo brain region : (a) RGB map of the in-vivo brain data from which the simulated data was created, (b) Ground truth ODF (without noise) corresponding to the boxed region in (a).

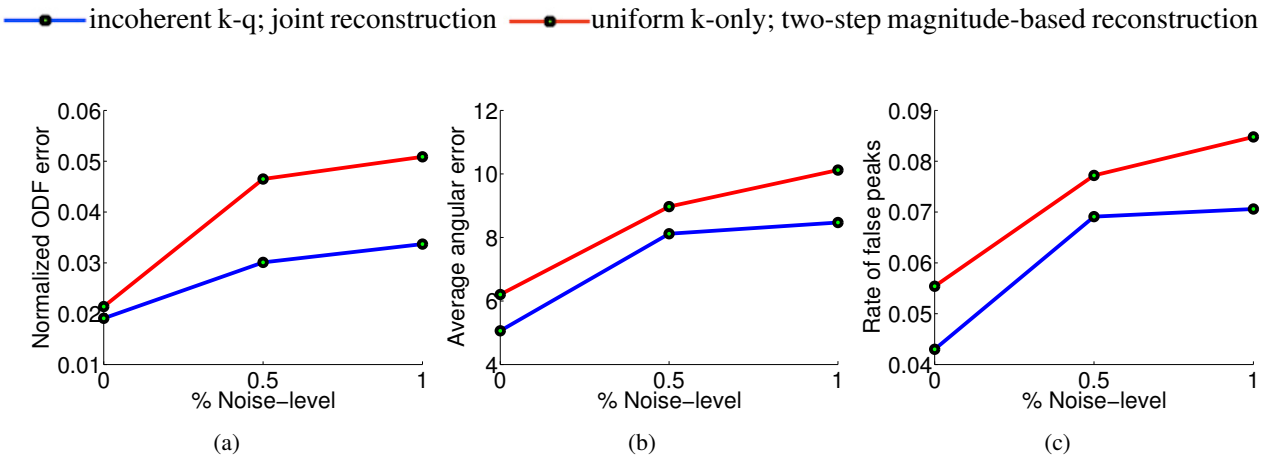

Figure 2: Effect of noise on reconstruction. The blue graph represents the joint reconstruction and the red graph represents the two-step magnitude based scheme. In the absence of noise, the two schemes shows similar performance. As noise level increases, the error in the two-step magnitude-based scheme increases because of the inaccurate noise modeling.

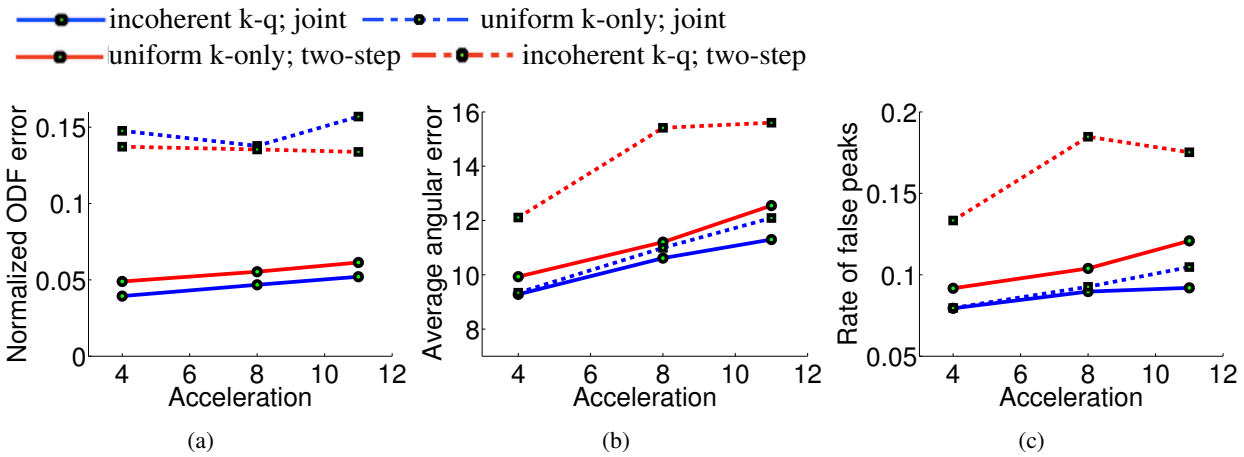

Figure 3: Effect of under-sampling pattern on reconstruction. The blue graph represents the joint reconstruction scheme that reconstructs the ODF directly from k-q data. The blue solid line represents the plots using the incoherent k-q under-sampling pattern and the blue dotted line represents plots using the uniform k-only under-sampling. The red graph represents the scheme that reconstructs the ODF using the two-step scheme. The red solid line represents the plots using the uniform k-only under-sampling pattern and the red dotted line represents plots using the incoherent k-q under-sampling pattern.

Supplementary Figure

Under-sampled Reconstruction of Non-diffusion Weighted Image for Various Accelerations

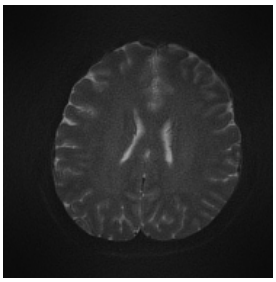

(a) fully-sampled

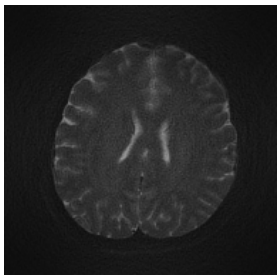

(b) R=2

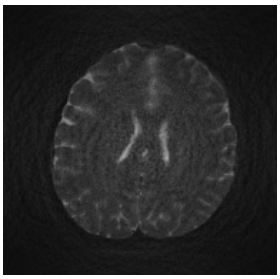

(c) R=4

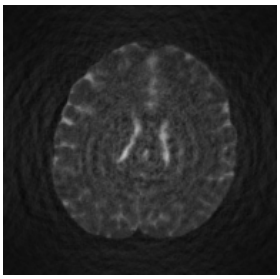

(d) R=8

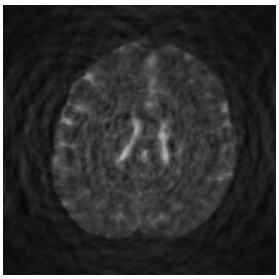

(e) R=11

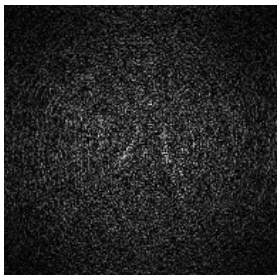

(f) error image for R=2

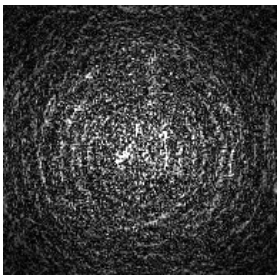

(g) error image for R=4

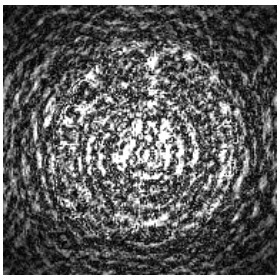

(h) error image for R=8

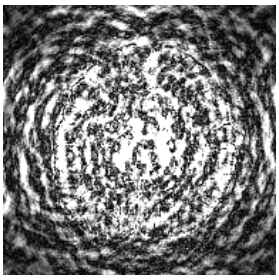

(i) error image for R=11

Figure 4: The effect of under-sampling demonstrated on the non-diffusion weighted image collected from dataset 2 using standard gridding reconstruction. (a) fully sampled reconstruction. (b) and (f) are the reconstruction from R=2 and its difference from the fully sampled image in (a). (c) and (g) are the reconstruction from R=4 and its difference from the fully sampled image in (a). (d) and (h) are the reconstruction from R=8 and its difference from the fully sampled image in (a). (e) and (i) are the reconstruction from R=11 and its difference from the fully sampled image in (a).